

Article

A gut-derived metabolite alters brain activity and anxiety behaviour in mice

<https://doi.org/10.1038/s41586-022-04396-8>

Received: 11 June 2020

Accepted: 2 January 2022

Published online: 14 February 2022

 Check for updates

Brittany D. Needham¹✉, Masanori Funabashi^{2,3}, Mark D. Adamo¹, Zhuo Wang⁴, Joseph C. Boktor¹, Jillian Haney⁵, Wei-Li Wu^{1,6,7}, Claire Rabut⁸, Mark S. Ladinsky¹, Son-Jong Hwang⁹, Yumei Guo⁴, Qiyun Zhu^{9,10}, Jessica A. Griffiths¹, Rob Knight^{9,11,12}, Pamela J. Bjorkman¹, Mikhail G. Shapiro⁸, Daniel H. Geschwind⁵, Daniel P. Holschneider^{4,13,14}, Michael A. Fischbach² & Sarkis K. Mazmanian¹✉

Integration of sensory and molecular inputs from the environment shapes animal behaviour. A major site of exposure to environmental molecules is the gastrointestinal tract, in which dietary components are chemically transformed by the microbiota¹ and gut-derived metabolites are disseminated to all organs, including the brain². In mice, the gut microbiota impacts behaviour³, modulates neurotransmitter production in the gut and brain^{4,5}, and influences brain development and myelination patterns^{6,7}. The mechanisms that mediate the gut–brain interactions remain poorly defined, although they broadly involve humoral or neuronal connections. We previously reported that the levels of the microbial metabolite 4-ethylphenyl sulfate (4EPS) were increased in a mouse model of atypical neurodevelopment⁸. Here we identified biosynthetic genes from the gut microbiome that mediate the conversion of dietary tyrosine to 4-ethylphenol (4EP), and bioengineered gut bacteria to selectively produce 4EPS in mice. 4EPS entered the brain and was associated with changes in region-specific activity and functional connectivity. Gene expression signatures revealed altered oligodendrocyte function in the brain, and 4EPS impaired oligodendrocyte maturation in mice and decreased oligodendrocyte–neuron interactions in ex vivo brain cultures. Mice colonized with 4EP-producing bacteria exhibited reduced myelination of neuronal axons. Altered myelination dynamics in the brain have been associated with behavioural outcomes^{7,9–14}. Accordingly, we observed that mice exposed to 4EPS displayed anxiety-like behaviours, and pharmacological treatments that promote oligodendrocyte differentiation prevented the behavioural effects of 4EPS. These findings reveal that a gut-derived molecule influences complex behaviours in mice through effects on oligodendrocyte function and myelin patterning in the brain.

The metabolite 4EPS was previously measured at a higher relative abundance in a mouse model of atypical neurodevelopment, and systemic delivery of synthetic 4EPS to naive mice altered their behaviour in the open-field test⁸. We recently reported that 4EPS is increased in the plasma of individuals with autism spectrum disorder (ASD)¹⁵, and show here that it is increased in the blood in the CNTNAP2 mouse model of ASD (Extended Data Fig. 1f). The gut microbiome is predicted to contain genes that convert tyrosine, the source of several mammalian neurotransmitters, to 4EP, which could then be sulfated¹⁶ to 4EPS by the host (Fig. 1a). Consistent with this notion, germ-free (GF) mice devoid

of a microbiota contain almost no detectable levels of 4EPS⁸ (Extended Data Fig. 1f). Some rare bacterial species in the Firmicutes phylum produce 4EP using *p*-coumaric acid as a substrate^{17,18}, and precursors of *p*-coumaric acid include tyrosine or plant-based molecules that can be metabolized by the gut microbiota to 4EP. Indeed, both a high-tyrosine fish-based diet and a soy-based diet resulted in measurable 4EPS levels in conventionally colonized mice (Extended Data Fig. 1g). By screening candidate gut bacterial isolates, we discovered that *Bacteroides ovatus* produces *p*-coumaric acid from tyrosine (Fig. 1b). Using the Basic Alignment Search Tool (BLAST), we identified a tyrosine ammonia lyase in

¹Division of Biology and Biological Engineering, California Institute of Technology, Pasadena, CA, USA. ²Department of Bioengineering and ChEM-H, Stanford University, Stanford, CA, USA.

³Translational Research Department, Daiichi Sankyo RD Novare Co Ltd, Tokyo, Japan. ⁴Department of Psychiatry and the Behavioral Sciences, Keck School of Medicine, University of Southern California, Los Angeles, CA, USA. ⁵Department of Neurology, University of California Los Angeles, Los Angeles, CA, USA. ⁶Department of Physiology, College of Medicine, National Cheng Kung University, Tainan, Taiwan. ⁷Institute of Basic Medical Sciences, College of Medicine, National Cheng Kung University, Tainan, Taiwan. ⁸Division of Chemistry and Chemical Engineering, California Institute of Technology, Pasadena, CA, USA. ⁹Department of Pediatrics, University of California San Diego, La Jolla, CA, USA. ¹⁰School of Life Sciences, Arizona State University, Tempe, AZ, USA. ¹¹Department of Computer Science and Engineering, University of California San Diego, La Jolla, CA, USA. ¹²Center for Microbiome Innovation, University of California San Diego, La Jolla, CA, USA. ¹³Department of Neurology, Keck School of Medicine, University of Southern California, Los Angeles, CA, USA. ¹⁴Viterbi School of Engineering, Department of Biomedical Engineering, University of Southern California, Los Angeles, CA, USA. ✉e-mail: bneedham@caltech.edu; sarkis@caltech.edu

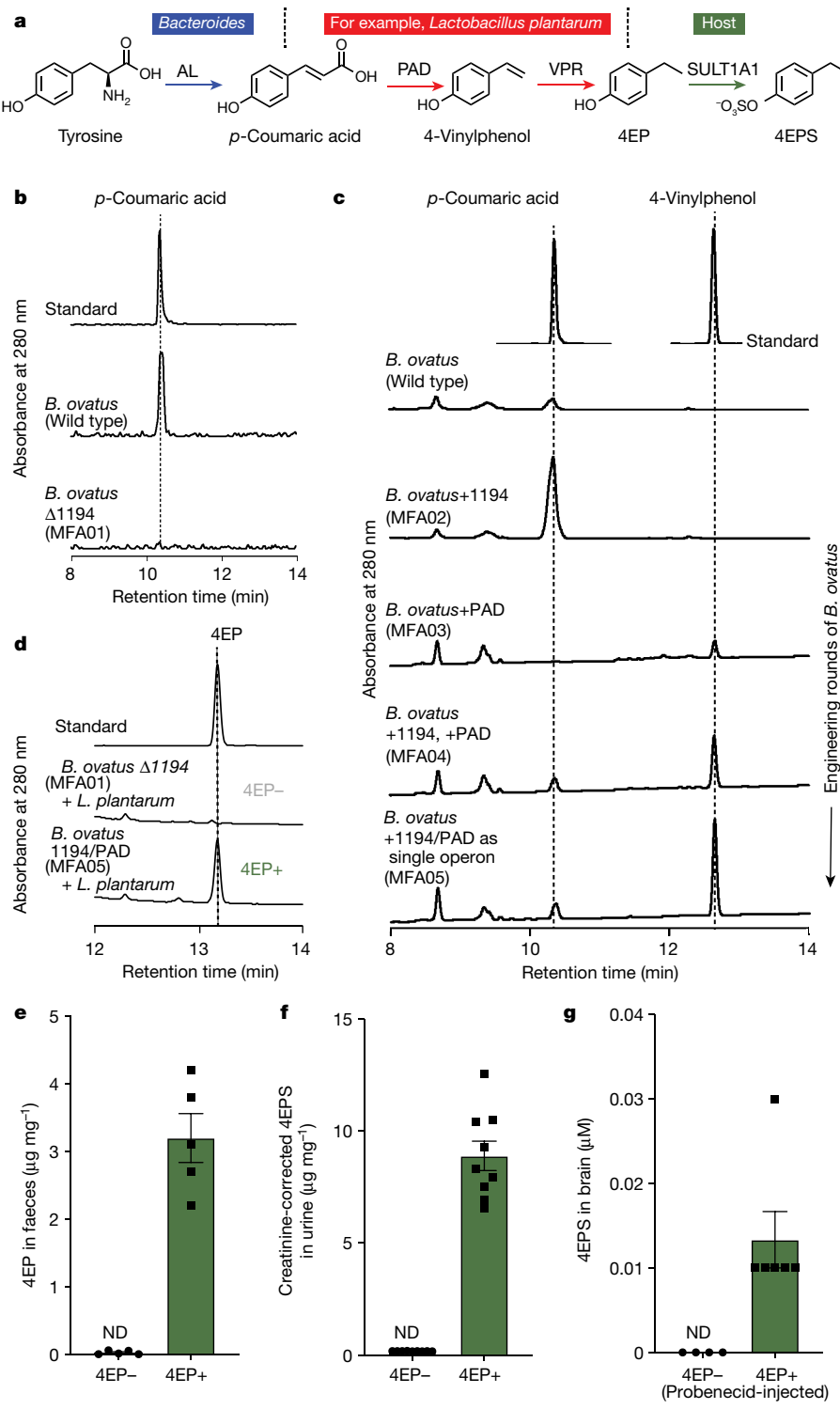


Fig. 1 | Discovery of a 4EP biosynthetic pathway, strain engineering of gut bacteria and colonization of mice to produce 4EPS. **a**, The proposed biosynthetic pathway of 4EP in gut bacteria through tyrosine ammonia lyase (AL, encoded by *BACOVA_01194*), phenolic acid decarboxylase (PAD) and vinyl phenol reductase (VPR) enzymes, and subsequent sulfation to 4EPS by host sulfotransferase (SULT1A1). The genes identified and cloned for bacterial strain engineering can convert tyrosine to 4EP through two chemical intermediates. **b, c**, 4EP precursors, *p*-coumaric acid and 4-vinylphenol from *in vitro* cultures of *B. ovatus* strains that were provided with tyrosine as a substrate. **b**, The conversion, or lack thereof, of tyrosine to *p*-coumaric acid by the *BACOVA_01194* gene product (AL/1194 in the figure) and deletion mutant (MFA01), respectively. **c**, The *BACOVA_01194* gene (AL/1194 in the figure) was introduced separately (MFA02), in addition to the *pad* gene (MFA04), or both genes as a single, highly expressed

operon (MFA05). Standards are shown at the top. Further details are provided in the Methods, Extended Data Fig. 1 and Supplementary Tables 1–3. **d**, 4EP levels from *in vitro* cultures (provided with tyrosine) of the 4EP[−] strain pair (*B. ovatus* Δ 1194 (MFA01) and *L. plantarum*) or the highest 4-vinylphenol-producing engineered strain, *B. ovatus*1194/PAD (MFA05) with *L. plantarum* (4EP⁺ strain pair). A standard is shown at the top. **e**, Levels of 4EP in faeces ($\mu\text{g per mg}$) of mice colonized with bacterial strains lacking (4EP[−]) and producing (4EP⁺) 4EP ($n = 5$). **f**, The levels of 4EPS in the urine of mice colonized with 4EP[−] or 4EP⁺ bacterial strains. Additional urine data are provided in Extended Data Fig. 1k. **g**, The brain levels of 4EPS (after injection with probenecid) in mice colonized with 4EP[−] ($n = 4$) and 4EP⁺ ($n = 6$) bacterial strains. Additional controls are shown in Extended Data Fig. 1f. At least two biologically independent trials were performed for each experiment. ND, not detectable. For **e–g**, data are mean \pm s.e.m.

B. ovatus (*BACOVA_01194*), the deletion of which abrogated the production of *p*-coumaric acid (Fig. 1b).

We co-colonized GF mice with *B. ovatus* and *Lactobacillus plantarum*, the latter of which can subsequently convert *p*-coumaric acid to 4EP¹⁸; however, the resulting 4EPS levels in urine were low (Extended Data Fig. 1f, h). To improve the efficiency of 4EP production, we performed several rounds of strain engineering (Methods). In brief, an extra copy of the first two genes in the pathway, *BACOVA_01194* and the phenolic acid decarboxylase (*pad*), were inserted into *B. ovatus* as a single, highly expressed operon (Fig. 1c). The engineered *B. ovatus* strain MFA05 robustly converts tyrosine to the intermediate 4-vinylphenol (Fig. 1c, Extended Data Fig. 1a–e) and, in co-culture with *L. plantarum*, 4-vinylphenol is quantitatively metabolized to 4EP (Fig. 1d). By contrast, when the *B. ovatus* Δ1194 mutant was co-cultured with *L. plantarum*, no 4EP was detected (Fig. 1d). We found homologues of each gene in ~25 genomes of sequenced human gut microorganisms, indicating that common pathways may be intact in the human microbiome (Extended Data Fig. 1i).

Gut-derived 4EPS in the circulation and brain

We colonized separate groups of GF mice with either of the engineered pairs of strains, which are represented in Fig. 1d, generating either 4EP⁺ or 4EP⁻ mice. As expected, 4EP was detected in the faeces (Fig. 1e), and its host-sulfated derivative, 4EPS, was detected in the serum and urine of 4EP⁺ colonized mice (Fig. 1f, Extended Data Fig. 1j). 4EP was undetectable in the serum of 4EP⁻ mice, suggesting efficient sulfation to 4EPS (Extended Data Fig. 1j). By contrast, 4EP⁻ mice do not have measurable levels of 4EP or 4EPS (Fig. 1e, f, Extended Data Fig. 1j). 4EPS was detectable in the brains of 4EP⁺ mice that were treated with probenecid, which inhibits organic anion transporters that mediate efflux of small molecules through the blood–brain barrier, suggesting accumulation of 4EPS in the brain (Fig. 1g, Extended Data Fig. 1k–m). We observed sulfation of 4EP to 4EPS by the sulfotransferase SULT1A1 and others during in vitro biochemical reactions (Extended Data Fig. 2a, b). SULT1A1 is found in intestinal, liver and brain tissues of mice (Extended Data Fig. 2c, d), although the sites of 4EP sulfation remain unknown.

4EP and 4EPS are phenolic molecules that may have toxic or inflammatory properties¹⁹. However, we observed no differences between the 4EP⁺ and 4EP⁻ groups in body weight or ambulatory activity (that is, locomotion) (Extended Data Fig. 2f, g). No evidence of intestinal dysfunction was detected in 4EP⁺ mice when assessing epithelial permeability (Extended Data Fig. 2h), faecal output (Extended Data Fig. 2i) or gross histopathology (Extended Data Fig. 2j). Bacterial colonization levels and ultrastructural localization of bacteria were similar between groups of mice (Extended Data Fig. 2k–m). We did not observe pro-inflammatory cytokine responses in colonic tissue or serum (Extended Data Fig. 3a, b), and observed only modest changes in peripheral immune cell proportions (Extended Data Fig. 3c, d). Cytokine levels trended towards an anti-inflammatory profile in the brain, with no signatures of microglial activation in 4EP⁺ mice (Extended Data Fig. 3e–g). Collectively, these studies establish a simplified animal model that reproduces the natural route of exposure to a gut microbial metabolite associated with altered behaviours (Extended Data Fig. 2e).

4EPS-dependent brain activity patterns

Although 4EP or 4EPS (hereafter 4EP(S)) may have effects on various organs, we focused our study on the brain. Initially, to capture brain-wide differences between 4EP⁺ and 4EP⁻ mice, we performed functional ultrasound imaging (fUSi)—an *in vivo* method that measures resting-state cerebral blood volume variation to assess functional connectivity (Extended Data Fig. 4a). We observed altered (mostly increased) correlation of signalling patterns within 4EP⁺ mice compared with 4EP⁻ mice (Fig. 2a). These changes were primarily observed in subregions of the hippocampus, thalamus, amygdala, hypothalamus,

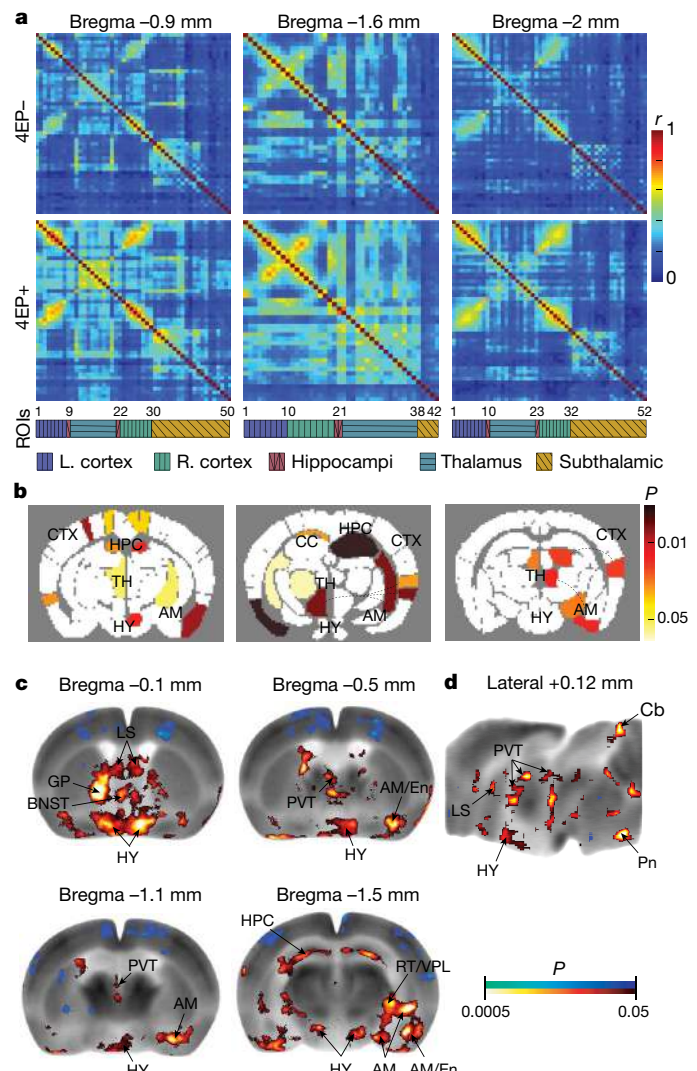


Fig. 2 | Functional brain connectivity and regional activation is altered in response to colonization by 4EP-producing bacteria. **a**, fUSi mean connectivity matrices correlating signal in brain regions⁴³ for each group, 4EP⁺ and 4EP⁻ ($n = 7$), and each coronal plane, bregma -0.9 mm, -1.6 mm and -2 mm. The Pearson correlation coefficient (r) is indicated by colour according to the key on the right. The location of regions of interest (ROIs) is categorized below; further details are provided in Extended Data Fig. 4a, b and Supplementary Table 4. **b**, Region pairs with significantly different connectivity in 4EP⁺ compared with 4EP⁻ groups. Region pairs are indicated by identically coloured P values (according to the key), and further indicated by dotted lines where necessary. Landmark brain regions are labelled in black, and specific ROIs are defined in Extended Data Fig. 4b and Supplementary Table 4. Analysis was performed using a paired t -test for each of the connectivity matrices with Bonferroni correction to control for multiple comparisons. **c, d**, Colour-coded overlays over representative coronal (**c**) and sagittal (**d**) sections of the mouse brain template showing significant differences in regional cerebral glucose uptake in 4EP⁺ mice compared with 4EP⁻ mice. $n = 11$. Statistical analysis was performed using t -tests; $P \leq 0.05$, extent threshold > 200 contiguous voxels, with both conditions met to be deemed significant. Red and blue indicate an increase and decrease, respectively, in glucose uptake in 4EP⁺ compared with 4EP⁻ mice. Two independent cohorts of mice from multiple litters were used for each experiment in the figure. AM, amygdala; Cb, cerebellar vermis; CC, corpus callosum; CTX, cortex; En, endopiriform; GP, globus pallidus; HPC, hippocampus; HY, hypothalamus; L, left; LS, lateral septum; Pn, pontine reticular nucleus; R, right; RT/VPL, reticular/ventral posterolateral thalamic nuclei; TH, thalamus.

piriform and cortex (Fig. 2b, Extended Data Fig. 4b), indicating that elevated 4EPS is associated with aberrant functional connectivity between various brain regions in mice.

To compare neural activity across the brain, we mapped glucose uptake where a systemically injected radiolabelled tracer ($[^{14}\text{C}]$ -2-deoxyglucose (2DG)) is rapidly incorporated into active brain regions. Changes in brain activity were evaluated by autoradiography analysis of brain sections comparing 4EP⁺ with 4EP⁻ mice. 4EP(S) was associated with increased glucose uptake in subregions of the hypothalamus (anterior area, lateral and paraventricular nucleus), amygdala (anterior, basolateral, central and cortical) and the bed nucleus of the stria terminalis (BNST), as well as in the paraventricular nucleus of the thalamus (PVT) (Fig. 2c, d). We also mapped uptake during a behavioural task (open-field exploration), in which we observed an overlap in increased activity in some regions (amygdala, hypothalamus, BNST and PVT), with differences in the spatial extent of these changes between stimuli conditions (Extended Data Fig. 4c–e). The regions highlighted by this analysis are important for a range of functions, including mediating appropriate responses to innate and learned fear stimuli^{20–23} and anxiety responses^{24,25}. We conclude that gut exposure to 4EP in mice results in altered functional connectivity and activity in multiple brain regions, including several that are associated with the limbic system.

Altered oligodendrocyte maturation

To resolve the molecular effects of 4EP(S) on the brain, we performed mRNA sequencing (QuantSeq) of six brain regions from 4EP⁺ and 4EP⁻ mice, including the PVT, basolateral amygdala, hypothalamus, BNST, medial prefrontal cortex (mPFC) and ventral hippocampus, resulting in tight clustering of transcriptomic profiles by brain region (Extended Data Fig. 5a). 4EP(S) predominantly affected global gene expression in the PVT, and the BNST and basolateral amygdala to a lesser extent (Fig. 3a, Extended Data Fig. 5b, e). Differentially expressed genes were aggregated into functional categories using annotated Gene Ontology (GO) terms, revealing that the Notch signalling pathway was elevated in the PVT of 4EP⁺ mice, whereas GO terms associated with dendrite and neuronal projection development were decreased (Extended Data Fig. 5c, d). Cell-specific enrichment analysis revealed decreased expression of genes specific to neurons, newly formed oligodendrocytes and mature oligodendrocytes in the PVT of 4EP⁺ mice compared with 4EP⁻ mice (Fig. 3b), suggesting that a potential decrease in development, abundance and/or activity of these cell types is associated with exposure to 4EP(S). Increased proliferation of immature oligodendrocytes and decreased differentiation into mature oligodendrocytes has been associated with elevated Notch signalling^{26,27}. Mature oligodendrocytes insulate neuronal projections with myelin, a fatty sheath that promotes the conduction of action potentials along axons²⁸. Accordingly, many genes that are hallmarks of mature oligodendrocytes, such as the myelin oligodendrocyte glycoprotein (*Mog*) and *Opalin* genes, were down-regulated in the PVT of 4EP⁺ mice, whereas several genes associated with non-myelinating, oligodendrocyte progenitor cells were elevated (Fig. 3c, Extended Data Fig. 5f, Supplementary Information). Using seed analysis of the 2DG-uptake data²⁹, we observed fewer significant correlations between the PVT and the rest of the brain in the 4EP⁺ group (168,042 voxels) compared with the 4EP⁻ group (271,392 voxels), an effect that is largely driven by the reduced number of positive correlations in the 4EP⁺ group compared with the 4EP⁻ group (61,572 versus 141,493 voxels) (Fig. 3d, Extended Data Fig. 5g).

We tested the hypothesis that 4EP(S) impacts oligodendrocyte maturation. Immunostaining in the PVT revealed increased expression of neural/glial antigen 2 (NG2) in 4EP⁺ mice, indicative of immature, oligodendrocyte precursor cells, along with decreased levels of a mature oligodendrocyte marker stained by anti-CC1 antibodies (Fig. 3e, f, Extended Data Fig. 5h–o). Analysis using flow cytometry and western blotting corroborated a skewing towards immature oligodendrocytes

in 4EP⁺ mice (Fig. 3g, h, Extended Data Fig. 6a–c). The levels of NeuN, a pan-neuronal marker, and OLIG2, a pan-oligodendrocyte marker, were unchanged (Extended Data Fig. 5k–n), indicating effects on oligodendrocyte maturation by 4EP(S) rather than a change in the total number of cells within this lineage. These data suggest that 4EP(S) exposure leads to reduced oligodendrocyte maturation.

Similar phenotypes were observed in organotypic brain slices cultured in the presence of 4EPS. 4EPS-treated ex vivo brain tissue showed increased levels of the early oligodendrocyte marker NG2 relative to the mature marker CC1 (Fig. 3i, Extended Data Fig. 6d), and reduced colocalization of myelin with neuronal axons (Fig. 3j, k, Extended Data Fig. 6e). Furthermore, functional markers of mature oligodendrocytes (MOG and myelin basic protein (MBP)) were lower in 4EPS-treated samples, whereas transcription of the gene encoding NG2 (*Cspg4*) was increased (Fig. 3l, Extended Data Fig. 6f, g). Although 4EPS enters the brain and has direct effects on brain tissue, we cannot exclude peripheral influences.

Reduced neuronal myelination in 4EP⁺ mice

We used electron microscope tomography to examine the ultrastructure of myelin in the dense and organized axonal tracts of the corpus callosum to facilitate myelin quantification. We observed a striking increase in the ratio of unmyelinated to myelinated axons in the brains of 4EP⁺ mice compared to 4EP⁻ mice (Fig. 4a, d), and a decrease in normalized (indicated by an increased *g*-ratio, or ratio between the inner and outer diameters of the myelin sheath) and actual myelin thickness in 4EP⁺ mice (Fig. 4b–d, Extended Data Fig. 7a–e). Thus, consistent with the decrease in mature oligodendrocytes, 4EP(S) exposure reduces myelination frequency and efficiency in the brain.

Diffusion tensor imaging, a magnetic resonance imaging modality that assesses diffusion along myelinated tracts in the brain, was used to investigate the structural connectivity of myelin between the PVT and the rest of the brain. We found lower fractional anisotropy—an indication of more dispersive rather than linear/restricted diffusion—in 4EP⁺ mice compared with 4EP⁻ mice (Fig. 4e and Extended Data Fig. 7f). A similar defect in myelination was observed in whole brains and trended in the corpus callosum (Extended Data Fig. 7g–i). The importance of altered myelin dynamics and brain connectivity is an emerging concept in behavioural neuroscience^{10–12,30,31}.

4EP(S) increases anxiety-like behaviour

Our previous study⁸ and the 4EP(S)-dependent changes in the limbic system observed here prompted us to investigate whether 4EP production in the gut can modulate complex behaviours in mice. 4EP(S) promoted robust anxiety-like behaviour in several testing paradigms: (1) the elevated plus maze (EPM), in which 4EP⁺ mice spend less time in the terminus of the open arms; (2) open-field exploration, in which mice ventured less into the more-exposed zone of the arena; and (3) the light/dark box, in which 4EP⁺ mice spent more time in the dark (Fig. 4f, g, Extended Data Fig. 8a–c). 4EP⁺ mice also displayed increased marble burying, reflecting features of anxiety and/or stereotypic behaviours, but no increase in self-grooming (Fig. 4h, Extended Data Fig. 8d). Beyond anxiety-like behaviours, 4EP⁺ mice exhibited modestly altered social communication with increased anogenital sniffing in the direct social interaction assay (Extended Data Fig. 8e). In the adult ultrasonic vocalization test, male 4EP⁺ mice emit significantly fewer auditory communications to a new age-matched female (Extended Data Fig. 8f). Interestingly, there were no significant differences in cognition or motor function between the groups (on the basis of novel object recognition, Y-maze alternation, beam traversal, pole descent or wire hang tests) (Extended Data Fig. 8g–k), further suggesting that the effects of 4EP(S) are selective for emotional behaviours. Our reductionist model system uses an artificial microbiome to study the effects of a gut microbial

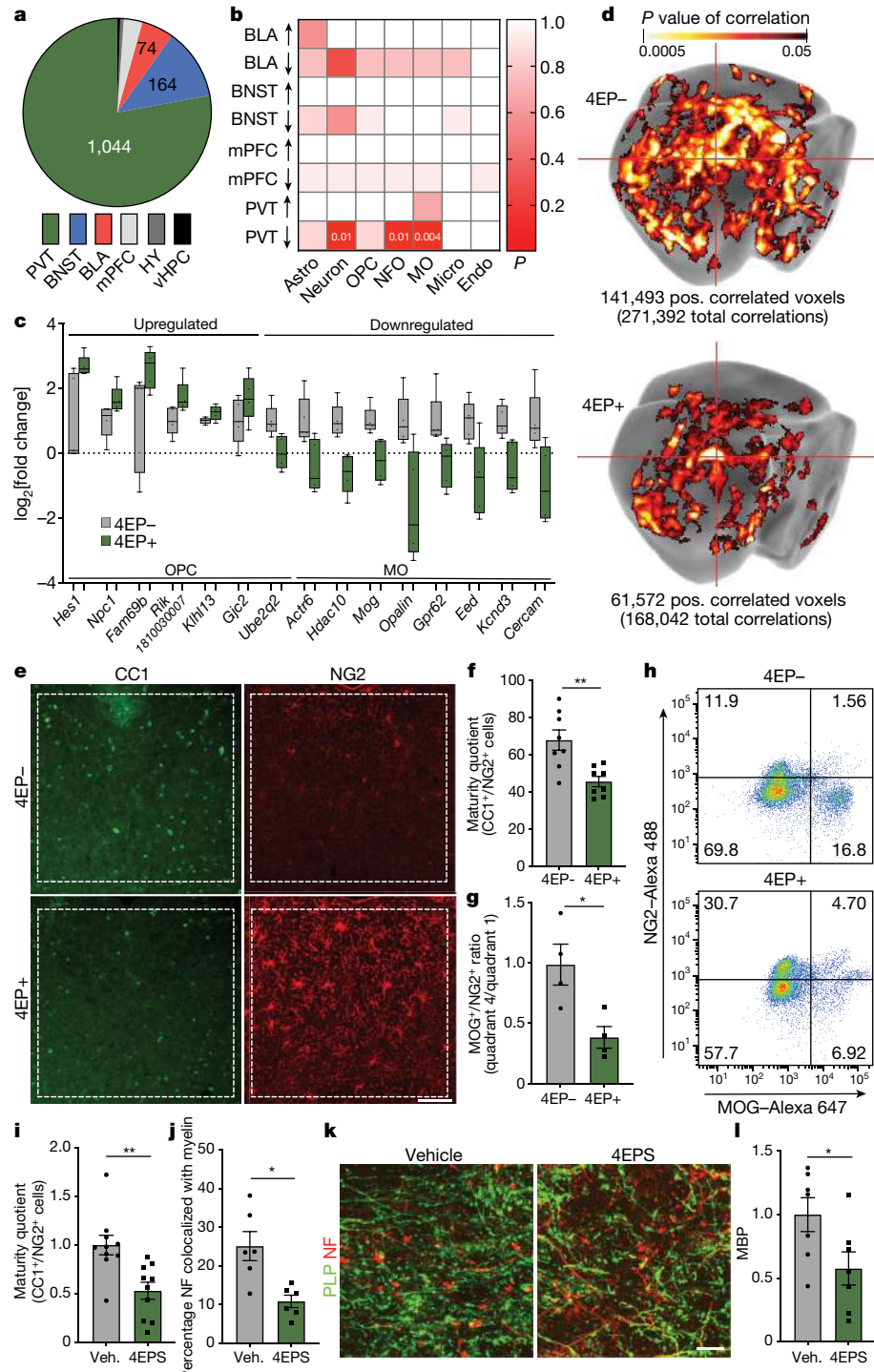


Fig. 3 | Reduced oligodendrocyte maturation in 4EP⁺ mice. **a**, The number of differential genes in brain regions ($n=5$) of baseline mice, determined using QuantSeq. Statistical analysis was performed using one-way analysis of variance (ANOVA) with Tukey test. **b**, Cell-specific enrichment analysis; $P<0.05$ is shown in red cells with white values. **c**, Representative subset of differential oligodendrocyte progenitor cells (OPCs) and mature oligodendrocyte genes. Statistical analysis was performed using one-way ANOVA with Tukey test. The box limits show the 25th to 75th percentiles, the centre line shows the median, and the whiskers show the minimum and maximum points. $n=5$. **d**, Whole-brain correlation to PVT seed using 2DG uptake data. $n=11$. The PVT (red cross-section) is indicated. Statistical analysis was performed using one-tailed multiple linear regression with a minimum threshold of 200 contiguous voxels with $P<0.05$. Pos., positive. **e**, Representative images of brain sections from 4EP⁻ and 4EP⁺ mice; NG2 (red) and CC1 (green). Scale bar, 100 μ m. **f**, Maturity quotient of oligodendrocytes in the PVT. $n=8$ cumulative totals used from biologically independent mice. $P=0.004$.

g, Quantitative flow cytometry analysis of PVT cells comparing the MOG⁺ quadrant 4 population over the NG2⁺ quadrant 1 population. $n=4$ pools of 5 PVTs. $P=0.03$. **h**, Representative flow plots. **i–l**, Organotypic brain slices treated with 10 μ M 4EPS. Each data point represents separate biological replicates. **i**, Maturity quotient of oligodendrocytes, using the total cumulative counts from 3–5 images per replicate. $n=9$ (vehicle (veh.)) and $n=10$ (4EPS). $P=0.003$. **j**, The percentage colocalization of neurofilament (NF) and proteolipid protein (PLP) antibody staining. $n=6$. $P=0.01$. **k**, Representative images of the experiment in **j**. Scale bar, 20 μ m. **l**, Western blot analysis of MBP in slices. $n=6$. $P=0.04$. Astro, astrocyte; BLA, basolateral amygdala; CC1, adenomatous polyposis coli; Endo, endothelia; Micro, microglia; MO, mature oligodendrocytes; NFO, newly formed oligodendrocytes; vHPC, ventral hippocampus. The experiments in **a–l** included biologically independent mice from multiple randomized litters examined over one (**a–c**) or two experiments (**d–l**). Data are mean \pm s.e.m. For **e–l**, statistical analysis was performed using two-tailed Welch's *t*-tests; * $P\leq 0.05$, ** $P\leq 0.01$.

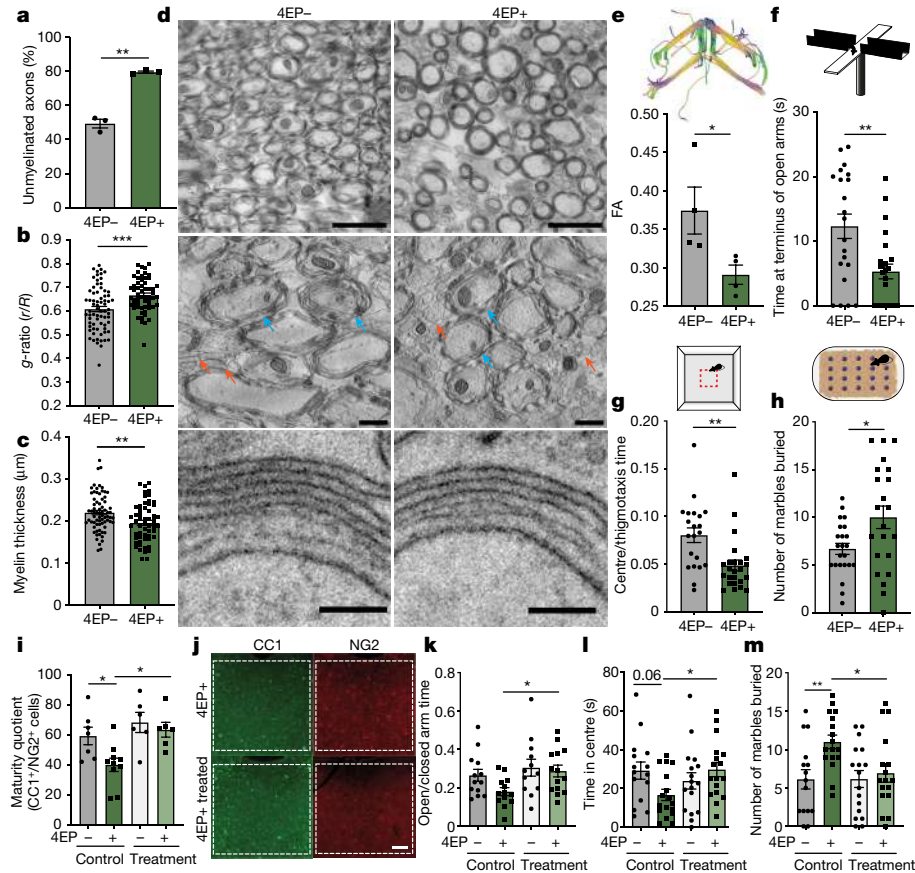


Fig. 4 | 4EP(S) alters myelination and anxiety-like behaviour. **a**, The percentage of unmyelinated axons. $n = 3$. Four images were scored from each biological replicate. $P = 0.005$. **b**, The g -ratio (r/R) of all axons ($n = 56$ (4EP⁻) and $n = 70$ (4EP⁺) axons). $n = 4$ mice. Four images were scored from each biological replicate. $P = 0.0001$. r , inner axonal diameter; R , outer myelinated diameter. **c**, The width of myelin ($n = 56$ (4EP⁻) and $n = 70$ (4EP⁺) axons). $n = 4$ mice. Four images were scored from each biological replicate. $P = 0.003$. **d**, Representative electron tomography images from $n = 4$ mice. Several myelinated and unmyelinated axons are marked by blue and orange arrows, respectively. **e**, Fractional anisotropy (FA) measured using diffusion tensor imaging. $n = 4$ mice. $P = 0.04$. Scale bars, 1 μm (top), 0.5 μm (middle) and 0.05 μm (bottom). **f**, EPM experiment: the time spent in the terminus (outer one-third) of the open arms. $n = 21$ (4EP⁻) and $n = 24$ (4EP⁺). $P = 0.003$. **g**, Open-field test. $n = 21$ (4EP⁻) and $n = 24$ (4EP⁺). $P = 0.002$. **h**, The number of marbles buried. $n = 24$ (4EP⁻) and $n = 23$ (4EP⁺). $P = 0.02$. **i**, The maturity quotient of oligodendrocytes in the PVT of 4EP⁻ and 4EP⁺ mice that were treated with or without clemastine fumarate. Cumulative totals used from individual mice: $n = 7$ (4EP⁻, control), $n = 10$ (4EP⁻, treated), $n = 6$ (4EP⁺,

control) and $n = 6$ (4EP⁺, treated). Control 4EP⁻ versus 4EP⁺: $P = 0.03$; 4EP⁺ control versus treatment: $P = 0.01$. **j**, Representative images of brain sections from mice that were treated with or without clemastine fumarate, stained for CC1 (green) and NG2 (red). **k–m**, Behavioural tests of mice (independent of cohorts used previously) that were treated with or without clemastine fumarate. **k**, EPM experiment. $n = 13$ (4EP⁻, control), $n = 13$ (4EP⁻, treated), $n = 12$ (4EP⁺, control) and $n = 14$ (4EP⁺, treated). 4EP⁻ control versus treatment: $P = 0.05$. **l**, Open-field test. $n = 15$ (4EP⁻, control), $n = 17$ (4EP⁻, treated), $n = 17$ (4EP⁺, control) and $n = 17$ (4EP⁺, treated). $P = 0.04$. **m**, The number of marbles buried. $n = 15$ (4EP⁻, control), $n = 17$ (4EP⁻, treated), $n = 17$ (4EP⁺, control) and $n = 17$ (4EP⁺, treated). Control 4EP⁻ versus 4EP⁺: $P = 0.009$; 4EP⁺ control versus treatment: $P = 0.03$. Biologically independent mice from multiple randomized litters examined over two experiments were used for all of the experiments. For **a–m**, data are mean \pm s.e.m. Statistical analysis was performed using two-tailed Welch's t -tests (**a–h**) or two-way ANOVA with Dunnett test for multiple comparisons to the 4EP⁺ control group (**i–m**); * $P \leq 0.05$, ** $P \leq 0.01$, *** $P \leq 0.001$.

metabolite (Extended Data Fig. 8*l*). Importantly, however, oral administration of 4EP(S) to elevate levels in conventionally colonized mice also increased anxiety-like behaviours and reduced oligodendrocyte maturation (Extended Data Fig. 9*a–j*). 4EP⁻ mice behaved similarly to conventionally colonized control mice (Extended Data Fig. 9*k, l*), indicating that the behavioural effects of 4EP(S) are not specific to gnotobiotic mice.

Finally, we sought to determine whether the 4EP(S)-mediated effects on oligodendrocytes contribute to altered behaviours. Administration of clemastine fumarate, a drug that promotes oligodendrocyte maturation³², increased mature oligodendrocyte ratios in 4EP⁺ mice as measured by CC1 and NG2 staining of brain sections (Fig. 4*i, j*, Extended Data Fig. 10*a*). Notably, enhancing maturation of oligodendrocytes prevented behavioural changes in 4EP⁺ mice, including alterations in EPM, open-field and the marble-burying tests (Fig. 4*k–m*, Extended Data Fig. 10*c, e, f*). We observed similar improvements in anxiety-like

behaviours with another myelination-inducing drug—miconazole (Extended Data Fig. 10*b, d, g–i*). We conclude that 4EP(S) impacts anxiety-like behaviours in mice in a manner that includes effects on oligodendrocyte maturation.

Discussion

Here we discovered a biosynthetic pathway for the production of the gut microbial metabolite 4EP. Although this pathway can use tyrosine as a precursor, we show that other dietary sources can also be metabolized by the gut microbiota into 4EP, and expect that, in humans, diverse dietary and microbial community structures may impact circulating metabolite levels. We also show that 4EP is sulfated and 4EPS enters the brains of mice, is associated with altered activation and connectivity of specific brain regions, and disrupts the maturation of oligodendrocytes and myelination patterns in the brain. Environmental cues are known

to have regional effects on oligodendrocyte–neural interactions, influencing brain circuits that govern particular behaviours^{6,7}. Although other brain regions are probably involved in the 4EP(S) response, as we detect broad changes to activation patterns, the PVT receives sensory and cognitive input, integrates these cues locally, and exports finely tuned signals to cortical and subcortical areas resulting in applied behavioural responses³³. Indeed, we show that gut exposure to 4EP alters several emotional, but not non-emotional, behaviours in mice. Future work will focus on uncovering how 4EPS leads to changes in oligodendrocyte maturation and myelination, defining brain regions that are causally affected and examining how myelination changes impact behaviour. Our data do not resolve whether 4EPS is the neuroactive metabolite, versus 4EP or unknown breakdown products. Identification of gut-derived microbial metabolites that enter the brain and affect brain activity defines an environmental influencer of anxiety-like behaviours.

Gut bacteria can synthesize classical neurotransmitters, such as dopamine, norepinephrine, serotonin and gamma-aminobutyric acid, and the production of new classes of neuroactive metabolites by the microbiome has been postulated³⁴. Molecules with phenolic structures similar to 4EP(S) are dysregulated in several preclinical models of behaviour^{8,35,36} as well as in certain neuropsychiatric disorders^{37–41}. Notably, a metabolite of tyrosine that is closely related to 4EP, *p*-cresol, has been suggested to influence oligodendrocyte function and affect social and depression-like behaviours in mice^{6,42}. Increased 4EPS is associated with abnormal repetitive behaviour in non-human primates³⁶, and plasma levels of 4EPS are significantly increased in a subset of individuals with ASD¹⁵. Moreover, the relative abundances of several related metabolites, such as 2-ethylphenylsulfate, 4-allylphenyl sulfate and 4-methylbenzenesulfonate, are altered in this same cohort¹⁵. We propose the hypothesis that 4EP(S) represents the archetypical example of a neuroactive microbial molecule that impacts brain activity and complex behaviours in animals, conceptually similar to mammalian neurotransmitters that regulate nervous system function.

Online content

Any methods, additional references, Nature Research reporting summaries, source data, extended data, supplementary information, acknowledgements, peer review information; details of author contributions and competing interests; and statements of data and code availability are available at <https://doi.org/10.1038/s41586-022-04396-8>.

- Sharon, G. et al. Specialized metabolites from the microbiome in health and disease. *Cell Metab.* **20**, 719–730 (2014).
- Swann, J. R. et al. Application of 1H NMR spectroscopy to the metabolic phenotyping of rodent brain extracts: a metabolicomic study of gut microbial influence on host brain metabolism. *J. Pharm. Biomed. Anal.* **143**, 141–146 (2017).
- Vuong, H. E., Yano, J. M., Fung, T. C. & Hsiao, E. Y. The microbiome and host behavior. *Annu. Rev. Neurosci.* **40**, 21–49 (2017).
- Needham, B. D., Kaddurah-Daouk, R. & Mazmanian, S. K. Gut microbial molecules in behavioural and neurodegenerative conditions. *Nat. Rev. Neurosci.* **21**, 717–731 (2020).
- Huang, F. & Wu, X. Brain neurotransmitter modulation by gut microbiota in anxiety and depression. *Front. Cell Dev. Biol.* **9**, 649103 (2021).
- Gacias, M. et al. Microbiota-driven transcriptional changes in prefrontal cortex override genetic differences in social behavior. *eLife* **5**, e13442 (2016).
- Hoban, A. E. et al. Regulation of prefrontal cortex myelination by the microbiota. *Transl. Psychiatry* **6**, e774 (2016).
- Hsiao, E. Y. et al. Microbiota modulate behavioral and physiological abnormalities associated with neurodevelopmental disorders. *Cell* **155**, 1451–1463 (2013).
- Berer, K. et al. Commensal microbiota and myelin autoantigen cooperate to trigger autoimmune demyelination. *Nature* **479**, 538–541 (2011).
- Pan, S., Mayoral, S. R., Choi, H. S., Chan, J. R. & Kheirbek, M. A. Preservation of a remote fear memory requires new myelin formation. *Nat. Neurosci.* **23**, 487–499 (2020).
- Maheras, K. J. et al. Absence of claudin 11 in CNS myelin perturbs behavior and neurotransmitter levels in mice. *Sci. Rep.* **8**, 3798 (2018).
- Bonnefil, V. et al. Region-specific myelin differences define behavioral consequences of chronic social defeat stress in mice. *eLife* **8**, e40855 (2019).
- Galvez-Contreras, A. Y., Zarate-Lopez, D., Torres-Chavez, A. L. & Gonzalez-Perez, O. Role of oligodendrocytes and myelin in the pathophysiology of autism spectrum disorder. *Brain Sci.* **10**, 951 (2020).
- Cassoli, J. S. et al. Disturbed macro-connectivity in schizophrenia linked to oligodendrocyte dysfunction: from structural findings to molecules. *npj Schizophrenia* **1**, 15034 (2015).
- Needham, B. D. et al. Plasma and fecal metabolite profiles in autism spectrum disorder. *Biol. Psychiatry* **89**, 451–462 (2020).
- Gamage, N. et al. Human sulfotransferases and their role in chemical metabolism. *Toxicol. Sci.* **90**, 5–22 (2006).
- Chamkha, M., Garcia, J. L. & Labat, M. Metabolism of cinnamic acids by some Clostridiales and emendation of the descriptions of *Clostridium aerotolerans*, *Clostridium celerecrescens* and *Clostridium xylanolyticum*. *Int. J. Syst. Evol. Microbiol.* **51**, 2105–2111 (2001).
- Santamaría, L., Reverón, I., Felipe, F. L. D., Rivas, B. D. L. & Muñoz, R. Ethylphenol Formation by *Lactobacillus plantarum*: identification of the enzyme involved in the reduction of vinylphenols. *Appl. Environ. Microbiol.* **84**, e01064–18 (2018).
- Agency for Toxic Substances and Disease Registry (ATSDR). Toxicological Profile for Cresols (CDC, 2008); <https://www.cdc.gov/TSP/ToxProfiles/ToxProfiles.aspx?id=946&id=196>
- Penzo, M. A. et al. The paraventricular thalamus controls a central amygdala fear circuit. *Nature* **519**, 455–459 (2015).
- Ahrens, S. et al. A central extended amygdala circuit that modulates anxiety. *J. Neurosci.* **38**, 5567–5583 (2018).
- Duval, E. R., Javanbakht, A. & Liberzon, I. Neural circuits in anxiety and stress disorders: a focused review. *Ther. Clin. Risk Manag.* **11**, 115–126 (2015).
- Robinson, O. J., Pike, A. C., Cornwell, B. & Grillon, C. The translational neural circuitry of anxiety. *J. Neurol. Neurosurg. Psychiatry* **90**, 1353–1360 (2019).
- Barson, J. R., Mack, N. R. & Gao, W.-J. The paraventricular nucleus of the thalamus is an important node in the emotional processing network. *Front. Behav. Neurosci.* **14**, 598469 (2020).
- Kirouac, G. J. The paraventricular nucleus of the thalamus as an integrating and relay node in the brain anxiety network. *Front. Behav. Neurosci.* **15**, 627633 (2021).
- Park, H.-C. & Appel, B. Delta-notch signaling regulates oligodendrocyte specification. *Development* **130**, 3747–3755 (2003).
- Wang, S. et al. Notch receptor activation inhibits oligodendrocyte differentiation. *Neuron* **21**, 63–75 (1998).
- Williamson, J. M. & Lyons, D. A. Myelin Dynamics Throughout Life: An Ever-Changing Landscape? *Front. Cell. Neurosci.* **12**, 424 (2018).
- Holschneider, D. P., Wang, Z. & Pang, R. D. Functional connectivity-based parcellation and connectome of cortical midline structures in the mouse: a perfusion autoradiography study. *Front. Neuroinform.* **8**, 61 (2014).
- Kaller, M. S., Lazar, A., Blanco-Duque, C., Sampaio-Baptista, C. & Johansen-Berg, H. Myelin plasticity and behaviour—connecting the dots. *Curr. Opin. Neurobiol.* **47**, 86–92 (2017).
- Barak, B. et al. Neuronal deletion of Gtf2i, associated with Williams syndrome, causes behavioral and myelin alterations rescuable by a remyelinating drug. *Nat. Neurosci.* **22**, 700–708 (2019).
- Xie, D. et al. Clemastine improves hypomyelination in rats with hypoxic-ischemic brain injury by reducing microglia-derived IL-1 β via P38 signaling pathway. *J. Neuroinflammation* **17**, 57 (2020).
- Kirouac, G. J. Placing the paraventricular nucleus of the thalamus within the brain circuits that control behavior. *Neurosci. Biobehav. Rev.* **56**, 315–329 (2015).
- Sharon, G., Sampson, T. R., Geschwind, D. H. & Mazmanian, S. K. The central nervous system and the gut microbiome. *Cell* **167**, 915–932 (2016).
- Tian, P., Wang, G., Zhao, J., Zhang, H. & Chen, W. Bifidobacterium with the role of 5-hydroxytryptophan synthesis regulation alleviates the symptom of depression and related microbiota dysbiosis. *J. Nutr. Biochem.* **66**, 43–51 (2019).
- Koyama, H. et al. Effects of housing conditions on behaviors and biochemical parameters in juvenile cynomolgus monkeys (*Macaca fascicularis*). *Exp. Anim.* **68**, 195–211 (2019).
- Tian, J.-S. et al. A GC-MS urinary quantitative metabolomics analysis in depressed patients treated with TCM formula of Xiaoyaosan. *J. Chromatogr. B Analyt. Technol. Biomed. Life Sci.* **1026**, 227–235 (2016).
- Sankowski, B. et al. Higher cerebrospinal fluid to plasma ratio of *p*-cresol sulfate and indoxyl sulfate in patients with Parkinson's disease. *Clin. Chim. Acta* **501**, 165–173 (2020).
- Gabriele, S. et al. Urinary *p*-cresol is elevated in young French children with autism spectrum disorder: a replication study. *Biomarkers* **19**, 463–470 (2014).
- Neul, J. L. et al. Metabolic signatures differentiate Rett syndrome from unaffected siblings. *Front. Integr. Neurosci.* **14**, 7 (2020).
- Takesada, M., Miyamoto, E., Kakimoto, Y., Sano, I. & Kaneko, Z. Phenolic and indole amines in the urine of schizophrenics. *Nature* **207**, 1199–1200 (1965).
- Sun, C.-Y. et al. *p*-Cresol sulfate caused behavior disorders and neurodegeneration in mice with unilateral nephrectomy involving oxidative stress and neuroinflammation. *Int. J. Mol. Sci.* **21**, 6687 (2020).
- Franklin, K. & Paxinos, G. *The Mouse Brain in Stereotaxic Coordinates* (Elsevier Science, 2007).

Publisher's note Springer Nature remains neutral with regard to jurisdictional claims in published maps and institutional affiliations.

© The Author(s), under exclusive licence to Springer Nature Limited 2022

Article

Methods

Bacterial strains and culture conditions

All of the bacterial strains and plasmids used in this study are shown in Supplementary Tables 1 and 2. *B. ovatus* was cultured in brain–heart infusion (BHI) agar medium supplemented with 10% horse blood, tryptone yeast extract glucose (TYG) broth or minimal medium (MM) at 37 °C in an anaerobic chamber from Coy Laboratories^{44,45}. Tyrosine was supplied as a substrate during investigation of 4EP production. *L. plantarum* was cultured anaerobically in MRS medium (BD) at 37 °C. *Escherichia coli* strains were cultured aerobically in LB broth. When appropriate, the growth medium was supplemented with 100 µg ml⁻¹ carbenicillin, 25 µg ml⁻¹ erythromycin, 2 µg ml⁻¹ tetracycline, 200 µg ml⁻¹ gentamicin and 200 µg ml⁻¹ 5-fluoro-2'-deoxyuridine (FUdR).

Disruption of *BACOVA_01194* in *B. ovatus*

Using the NCBI BLAST alignment tools, we predicted that *BACOVA_01194* is an ammonia lyase that can metabolize tyrosine. For all of the PCR amplification steps, we used PrimeSTAR Max DNA polymerase (Takara Bio) according to the manufacturer's instructions. Primer sequences are shown in Supplementary Table 3. We used a previously reported double-crossover recombination method to construct *B. ovatus* Δ1194 (ref. ⁴⁶). In brief, -1 kb DNA fragments corresponding to the upstream and downstream regions of the target gene were PCR amplified and then digested with restriction endonucleases. The digested fragments were then ligated into the suicide plasmid pExchange-*tdk* using T4 DNA ligase (New England Biolabs). The resulting plasmid was transformed into *E. coli* S17-1λ pir by electroporation and transformants were confirmed by PCR amplification of the junction regions. An *E. coli* clone containing the plasmid was cultivated and plasmid DNA was isolated, purified and verified by DNA sequencing.

For conjugation into *B. ovatus*, *B. ovatus* Δ*tdk* and *E. coli* S17-1λ pir containing the plasmid were cultivated and the cells were collected by centrifugation. The cell pellets were washed with PBS to remove residual antibiotics and combined in TYG medium. The suspension was plated on BHI–blood agar medium without any antibiotics and cultivated aerobically at 37 °C for 1 day. The bacterial biomass was recovered by scraping and resuspended in TYG medium. The suspension was then plated on BHI–blood agar medium supplemented with erythromycin and gentamicin and single-crossover integrants were selected. These strains cultured in TYG medium overnight and plated on BHI–blood agar medium supplemented with FUdR. The deletion mutant was screened by PCR amplification and verified by DNA sequencing.

B. ovatus strain engineering

When a culture of *L. plantarum* was supplemented with 4-vinylphenol, it was converted quantitatively to 4-ethylphenol. By contrast, when the culture was supplemented with *p*-coumarate, the conversion to 4-vinylphenol was slow. This suggested that the decarboxylation step might be rate limiting for 4-ethylphenol biosynthesis in binary culture. To address this challenge, we introduced the *pad* gene from *L. plantarum* into *B. ovatus* to enable *B. ovatus* to produce 4-vinylphenol directly from tyrosine. However, the resulting strain did not produce 4-vinylphenol. We next introduced a second copy of the *BACOVA_01194* gene into *B. ovatus* along with *pad* in case the intermediate *p*-coumarate was limiting, but this strain failed to produce 4-vinylphenol. To address the possibility that the *pad* gene from *L. plantarum* does not function robustly in *B. ovatus*, *pad* from *Bacillus subtilis* was introduced into *B. ovatus*; the engineered strain produced 4-vinylphenol robustly from tyrosine. To boost the level of 4-vinylphenol, a second copy of *BACOVA_01194* was introduced into *B. ovatus* along with *pad* from *B. subtilis* using a second integration vector with a different antibiotic marker. This strain produced 4-vinylphenol more robustly. We then combined the second copy of *BACOVA_01194* and *pad* into a single artificial operon driven by a strong phage promoter and introduced

this construct into *B. ovatus*. Interestingly, this strain produced a much higher level of 4-vinylphenol and it was used throughout the manuscript for co-cultivation and colonization. Vector maps and sequences of primers used for *B. ovatus* engineering are shown in Extended Data Fig. 1 and Supplementary Table 3, respectively. The artificial operon was constructed using the following method: a phage promoter along with 5' and 3' flanking sequences from the target vector, pNBU2, and one of the target genes was amplified by PCR. The target gene with 5' and 3' flanking sequences containing sequences of the phage promoter and the pNBU2 vector were also amplified. These two PCR fragments were assembled by overlap PCR. The *BO_01194* and *pad* genes were each assembled by one more round of overlap PCR. The fragment containing the target gene and the phage promoter was cloned into the fragment of pNBU2 vector using Gibson Assembly. The assembled plasmids were transformed into *E. coli* S17-1λ pir competent cells by electroporation and the transformants were confirmed by PCR amplification of the junction regions. The positive clone containing the assembled plasmid was cultivated and the plasmid was isolated, purified and confirmed by DNA sequencing. To conjugate the plasmid into *B. ovatus*, *B. ovatus* Δ*tdk* and *E. coli* S17-1λ pir containing the plasmid were cultivated and the cells were collected. The cell pellets were washed with PBS to remove residual antibiotics and combined in TYG medium. The suspension was plated on BHI–blood agar medium without any antibiotics and grown aerobically at 37 °C for 1 day. The bacterial biomass was recovered by scraping and resuspended in TYG medium. The suspension was then plated on BHI–blood agar medium supplemented with erythromycin and gentamicin and antibiotic resistant strains were selected followed by PCR amplification of the junction regions.

Extraction of bacterial culture metabolites

For metabolite analysis, *B. ovatus* was cultured in TYG medium overnight and the cells were collected and washed with MM. The cell pellet was resuspended in MM containing 0.5 mg ml⁻¹ tyrosine to an optical density at 600 nm (OD₆₀₀) of 1.0 and incubated anaerobically for 1 day. The culture was extracted with acetone (20% v/v) and centrifuged. The supernatant was analysed using liquid chromatography coupled with mass spectrometry (LC–MS) as described below. For LC–MS analysis of co-culture experiments, *B. ovatus* and *L. plantarum* were cultivated anaerobically in TYG and MRS, respectively, overnight and the cells were collected and washed with MM. The cell pellet was resuspended in MM containing 0.5 mg ml⁻¹ tyrosine to OD₆₀₀ = 1.0 and combined in the same culture tube. After incubation for 1 day, the samples for high-performance LC (HPLC) analysis were prepared as described above.

LC–MS analysis of bacterial culture metabolites

Metabolite extracts were analysed using an Agilent 1260 LC system coupled to an Agilent 6120 quadrupole mass spectrometer with a 3 µm, 4.6 × 75 mm Unison UK-C18 column (Imtakt). Water with 10 mM ammonium acetate and 0.1% formic acid (A) and acetonitrile with 0.1% formic acid (B) was used as the mobile phase at a flow rate of 1.0 ml min⁻¹ with the following 20 min gradient: 0–5 min, 0% B; 5–17 min, 0–90% B; 17–20 min, 95% B. *p*-coumaric acid and 4-VP were detected at 280 nm and these retention times were -10.3 min and -12.6 min, respectively. The retention time of 4-EP was -7.6 min. Standards of *p*-coumaric acid and 4-ethyl phenol were purchased (Sigma-Aldrich).

Gene sequence alignment

Sequences of the genes used for strain engineering were aligned against the reference genomes in the WoL database, which were pre-annotated using UniRef release 2019_07. The annotation files are publicly available at GitHub (<https://biocore.github.io/wol/download>). The alignment used DIAMOND v.0.9.25 with all of the default parameters (diamond blastx-d/path/to/db-qinput.fa-o output.txt). The output files were then processed using Woltka (<https://github.com/qiyunzhu/woltka>),

which generated the taxonomic and functional (UniRef) profile of the three genes against the entire WoL genome catalogue.

Mouse husbandry

All animal husbandry and experiments were approved by the Caltech Institutional Animal Care and Use Committee. Throughout the study, mice were maintained in autoclaved microisolator cages with autoclaved bedding (Aspen Chip Bedding, Northeastern Products), water and chow (Laboratory Autoclavable Rodent Diet, 5010, LabDiet). Diets used in Extended Data Fig. 1g were purchased from Envigo Teklad, carbohydrate and fat content. The soy protein has ~300 ppm total isoflavones. The tyrosine levels are 4.6 g kg⁻¹ in soy diet and 17.1 g kg⁻¹ in fish diet. Specific pathogen free (SPF) C57BL/6J male mice (aged 8 weeks; Jackson Laboratory) were provided with these special diets for 2 weeks ad libitum before urine collection for metabolite analysis as described below.

Mice were maintained at an ambient temperature of 71–75 °F, 30–70% humidity, under a cycle of 13 h light and 11 h dark.

Experimental design of mouse experiments

GF C57BL/6J male weanlings (aged 3 weeks) from the Mazmanian laboratory colony were colonized by gavage of 100 µl of 1:1 mixture of 10⁹ colony-forming units per ml *B. ovatus* (±4EP pathway genes) and wild-type *L. plantarum*. This process was continually performed, yielding a steady schedule of cohorts for continued study throughout this work. The size of animal groups was determined by the largest number of pups that could be born within the space of the GF isolators. Weekly tests to confirm gnotobiotic status were performed and 4EPS levels were confirmed in the urine regularly. All of the experiments in the study were repeated on at least two independent cohorts. Preliminary behavioural analysis identified a stronger phenotype in males (Extended Data Fig. 10j–l); male mice were therefore used for the rest of the study to limit animal use.

16S sequencing was performed by Laragen and analysis was performed using a 16S V6 library. Paired-end fastq files were processed using Qiime2 (ref. ⁴⁷). In brief, sequences were quality-control processed using dada2 (ref. ⁴⁸), truncating reads to 150 bp. Taxonomic classification was then conducted using the greengenes database. Analysis was conducted on samples rarefied to 24,000 reads.

In the conventionally colonized (SPF) experiment, male weanlings (aged 3 weeks) were provided with 250 mM 4EP and 4EPS in drinking water (or vehicle). In these experiments, oral administration continued until endpoint. 4EPS was synthesized as previously described⁸, and 4EP was purchased from Sigma-Aldrich. When appropriate, beginning at 4–5 weeks of age, sterile clemastine fumarate (0.03 mg ml⁻¹) or DMSO vehicle (Sigma-Aldrich) was added to the drinking water and the water was changed every other day, or miconazole solution (40 mg kg⁻¹) or 3% DMSO vehicle was gavaged once daily. In all cases, behaviour testing started at 6 weeks of age.

Extraction of urine, faeces, serum and brain metabolites

Urine was collected by placing autoclaved aluminium foil under the mouse while briefly scruffing it, and then pipetting the urine from the foil. The urine was diluted fivefold with aqueous acetonitrile (50% v/v) and centrifuged. The supernatant was analysed using LC–MS to detect 4EPS. 4EPS for a standard was prepared as previously described⁸. Ethyl acetate was added to the supernatant to create a 1:1:1 mixture (v/v) of water, acetonitrile and ethyl acetate. After mixing and centrifugation, the organic layer was analysed using GC–MS to detect 4EP.

Faecal pellets were collected by placing the mouse briefly into a sterile plastic beaker. A 5× volume of 50% acetonitrile/water was added and the pellets were homogenized by bead beating, followed by centrifugation. The supernatant was analysed using LC–MS to detect 4EPS. To detect 4EP, the samples were extracted with ethyl acetate as described above.

Blood was collected by cardiac puncture followed by separation using Sarstedt Serum-Gel microtubes (Thermo Fisher Scientific) according to the manufacturer's specifications.

Brain tissue was collected by cardiac perfusion as described for immunohistochemistry but with PBS instead of PFA, then dissected. A 2× volume of 50% acetonitrile/water was added and the tissue was homogenized by bead beating, followed by centrifugation. The supernatant was directly injected for analysis by LC–MS to detect 4EPS.

LC–MS analysis of metabolites from the urine, serum and brain

Samples were analysed using an Agilent 1290 LC system coupled to an Agilent 6530 QTOF with a 3 µm, 4.6 × 75 mm Unison UK-C18 column using the same method described above. All data were collected in negative ion mode. 4EPS was detected as [M–H]⁻ (calculated *m/z* = 201.0227) and the retention time was ~7.9 min. 4EPS prepared previously was used as a standard⁸.

GC–MS analysis of metabolites from faeces

Samples were analysed using a split ratio of 10:1 using an Agilent 7890 GC coupled to an Agilent 5977 MSD with a HP-5MS fused silica capillary column (30 m × 250 µm × 0.25 µm). The injector temperature was set at 250 °C and high-purity helium gas was used as carrier at a constant flow rate of 1.0 ml min⁻¹. The column temperature was initially kept at 40 °C for 2 min, then increased to 100 °C at a rate of 40 °C min⁻¹, increased to 105 °C at a rate of 2 °C min⁻¹ and then raised to 320 °C at a rate of 30 °C min⁻¹, held for 3 min, giving 16.367 min in total. The retention time of 4-EP (calculated *m/z* = 122.07) was ~7.6 min.

Creatinine measurement

The concentration of creatinine was measured using Colorimetric Creatinine Assay Kit (Abcam) according to the manufacturer's instructions.

Brain levels of 4EPS

Probenecid (Invitrogen), an organic anion transporter (OAT) inhibitor that works on OAT1 and OAT3 was injected intraperitoneally (i.p.) into mice (120 mg kg⁻¹). After 1 h, whole brains were removed, homogenized and analysed as described above by LC–MS. For SPF mice, 30 min after the probenecid injection, either an i.p. injection of 100 µl of 8 mM 4EPS or an oral gavage of 160 mg kg⁻¹ 4EP (Sigma-Aldrich) was administered, then brains were collected after an additional 30 min or along 30 min time points. For mice colonized with 4EP⁻ and 4EP⁺ strains, mice were perfused with PBS before tissue collection to ensure that any metabolite detected was not simply due to levels in the blood.

qPCR

RNA was extracted using the RNeasy Mini Kit (Qiagen) and cDNA was transcribed using the iScript cDNA Synthesis Kit (Thermo Fisher Scientific). Quantitative PCR (qPCR) was performed using the SYBR master mix (Thermo Fisher Scientific); a list of the primers used is provided in Supplementary Table 5.

In vitro assays of 4EP sulfation

Recombinant sulfotransferases (sult1b1, 1c2, 1e1, 2a1 and 1a1) and the Universal Sulfotransferase Activity Kit (R&D Systems) were used according to the manufacturer's recommendations. After analysis by plate reader, samples were analysed by LC–MS as described above to confirm that the sulfated product was indeed 4EPS. Cytosolic fractions from 50–200 µg tissue containing endogenous sulfotransferases were extracted and tested for SULT activity on 4EP as previously described^{49,50} and analysed using LC–MS as described above.

Intestinal permeability

The FITC-dextran intestinal permeability assay was performed as described previously⁵¹ on 4EP⁻ and 4EP⁺ mice at nine weeks.

Article

H&E staining

Gut tissue was dissected immediately after euthanasia at nine weeks of age and fixed in neutral 10% formalin, paraffin embedded, sectioned and stained with haematoxylin and eosin (H&E) by Pacific Pathology.

Cytokine analysis

Tissue samples collected at nine weeks of age were homogenized by bead-beating in lysing matrix D tubes (MP Biomedicals) in RIPA buffer (Millipore) containing protease inhibitor tablets (Roche) followed by protein quantification and normalization using the Pierce BCA Protein Assay Kit (Thermo Fisher Scientific). Blood samples were collected by cardiac puncture followed by serum isolation in clotting tubes (Sarstedt). Using the Bio-Plex Pro Mouse Cytokine 23-plex assay (Bio-Rad) according to manufacturer's recommendations, cytokine and chemokine levels were determined using the Bio-Plex 200 Systems instrument. Undetected values were rare and, in those cases, were imputed with the lowest detected value from that cytokine. One-way ANOVA with correction for multiple comparisons was performed and significance is indicated by asterisks; * $P < 0.05$, ** $P < 0.01$, *** $P < 0.001$.

Microglial enrichment for qPCR

Brain samples were collected and single-cell suspensions were generated as described in the 'Flow cytometry' section below. Microglial-enriched populations were obtained using CD11b microbeads (Miltenyi Biotec).

Animal protocol for fUSi session

A total of 14 mice was imaged: 7 mice for the 4EP⁻ group and 7 for the 4EP⁺ group. Images were acquired through intact skull and skin after hair removal using a commercial depilatory cream (Nair, Church & Dwight) without any contrast agent injection. During handling (shaving, positioning) mice were anaesthetized with isoflurane (2%) administered in a mixture of 30% O₂ and 70% N₂. During the resting-state experiment, mice were sedated using dexmedetomidine (Tocris Bioscience). A bolus of 0.10 mg kg⁻¹ was injected subcutaneously, and isoflurane was discontinued after 5 min. Mice were head fixed on a stereotaxic frame to minimize brain motion during imaging. After a 90 min imaging session, mice were euthanized by cervical dislocation.

fUSi analysis

fUSi visualizes neural activity by mapping local changes in cerebral blood volume (CBV). CBV variations are tightly linked to neuronal activity through the neurovascular coupling⁵² and are evaluated by calculated power doppler variations in the brain⁵³. fUSi was performed transcranially as described previously⁵⁴ using a 15 MHz ultrasonic ultra-light probe prototype (15 MHz, 64 elements, 0.110 mm pitch, Vermon) connected to a Verasonics Vantage ultrasound system (Verasonics) driven by custom MATLAB (MathWorks) transmission scripts (https://github.com/brittanyneedham/Needham_Nature2022)⁵⁵. Each Power Doppler image was obtained from the temporal integration of 220 compounded frames acquired at 500 Hz frame rate, using 5 tilted plane waves separated by 3° (-6°, -3°, 0°, 3°, 6°) acquired at a 2,500 Hz pulse repetition frequency. Power Doppler images were then repeated every second (1 Hz image framerate). Each block of 220 images was processed using a SVD clutter filter⁵⁶ to separate tissue signal from blood signal to obtain a final Power Doppler image exhibiting CBV in the whole imaging plane. Three coronal planes per mice were scanned at a rate of 15 min imaging time per plane, respectively, bregma -0.9 mm, bregma -1.6 mm and bregma -2 mm.

Functional ultrasound data processing and statistics

Power Doppler data were collected continuously during the imaging session and connectivity process was applied afterwards. We followed the functional connectivity process on fUSi data described in Osmanski

et al.⁵⁷. For each coronal plane, for each acquisition and each mouse, first, a low-pass filter (cutting frequency, 0.2 Hz) was performed on the power Doppler temporal signals for each individual pixel of the image to remove high-frequency signals while preserving the resting-state frequency band. The signal was then detrended with a polynomial fit of order 4 to remove low frequencies that could bias the correlation value. Finally, the normal score of the temporal filtered signals was calculated to enable correlation calculation. To build functional connectivity matrices, we determined within each coronal plane ROIs defined from the Paxinos Atlas⁴³ (see Extended Data Fig. 2a for ROIs mapping in each plane). The Pearson correlation of the filtered signals of each pair of ROIs within a same plane was then calculated and the corresponding correlation values were stored in the cells in which the regions intersect in the connectivity matrix. Figure 2 shows the mean connectivity matrices from each coronal plane (bregma -0.9 mm, bregma -1.6 mm and bregma -2 mm) of each studied group (4EP⁻ and 4EP⁺). Within the same coronal plane, cells of the connectivity matrices from the 4EP⁻ and 4EP⁺ groups were statistically analysed individually using a paired *t*-test. Multiple-comparison correction was performed using Bonferroni correction⁵⁸. Region pairs that showed significant differences between groups are shown in Fig. 2c.

ROI distribution graphs of each coronal plane are provided. Coronal plane bregma -0.9 mm: ROIs 1 to 8 are located in the left cortex, ROI 9 is the left hippocampus, ROIs 11 to 21 are located in the thalamus, ROI 22 is the right hippocampus, ROIs 23 to 30 are located in the right cortex and, finally, ROIs 31 to 48 are subthalamic regions. Coronal plane bregma -1.6 mm: ROIs 1 to 20 are located in the cortex, ROIs 21 and 22 are the left and right hippocampi, ROIs 23 to 38 are located in the thalamus and ROIs 39 to 42 are subthalamic regions. Coronal plane bregma -2 mm: ROIs 1 to 9 are located in the left cortex, ROI 10 is the left hippocampus, ROIs 11 to 22 are located in the thalamus, ROI 23 is the right hippocampus, ROIs 24 to 32 are located in the right cortex and, finally, ROIs 33 to 50 are subthalamic regions.

Autoradiography brain mapping

The autoradiographic 2DG uptake method is a well-established, time-tested approach to functional brain mapping based on a tight coupling between neural activity and metabolism. It is particularly suitable in awake, free-moving mice, and complements the fUSi approach. Male mice colonized as described above were housed in pairs from weaning. Mapping of cerebral glucose metabolism was performed as described previously^{59,60} in four groups: 4EP⁺/home cage ($n = 11$), 4EP⁺/open field ($n = 11$), 4EP⁻/home cage ($n = 10$), 4EP⁻/open field ($n = 11$). The experiment was performed in two cohorts with balanced group assignment in each cohort. At 7 weeks mice were habituated to handling for 5 min each day for 3 days before 2DG mapping. They were brought in their home cages to the experimental suite 16 h before mapping and were fasted of food overnight with water ad libitum. A pair of mice from the same home cage were administered i.p. [¹⁴C]-2-deoxy-D-glucose (MC355, radiochemical purity > 97%, specific activity 45–60 mCi mmol⁻¹, Moravek) at 0.3 µCi g⁻¹ bodyweight in 0.5 ml normal saline. The mice were placed back in their home cage for 5 min. One mouse was then placed into the open-field arena and allowed to explore the arena for 45 min to allow uptake of the tracer, while the other remained in the home cage. At the end of exposure, after cervical dislocation, the brains were extracted and flash-frozen in methylbutane over dry ice (around -55 °C) and later serially sectioned into 20-µm slices in a cryostat at -20 °C (Mikron HM550 OMP, Thermo Fisher Scientific). Slices were heat-dried on glass slides and exposed to Kodak Biomax MR diagnostic film (Eastman Kodak) for 3 days at room temperature. Autoradiographs were then digitized on an 8-bit grey scale using a voltage-stabilized light box (Northern Lights Illuminator, InterFocus) and a Retiga 4000R charge-coupled device monochrome camera (Qimaging).

Relative regional cerebral glucose uptake (rCGU) was measured and analysed on a whole-brain basis using Statistical Parametric Mapping

(SPM, version 5, Wellcome Centre for Neuroimaging, University College London) as previously described^{59,61}. In brief, each three-dimensional (3D) brain was reconstructed from 68 digitized autoradiographs (voxel size: $40 \times 140 \times 40 \mu\text{m}$) using TurboReg, an automated pixel-based registration algorithm implemented in ImageJ (v.1.35, <http://rsbweb.nih.gov/ij/>). This algorithm registered each section sequentially to the previous section using a non-warping geometric model that included rotations, rigid-body transformation and nearest-neighbour interpolation. One ‘artifact free’ mouse brain was selected as a reference, and all brains were spatially normalized to the reference in SPM. Spatial normalization consisted of applying a 12-parameter affine transformation followed by a nonlinear spatial normalization using 3D discrete cosine transforms. All normalized brains were then averaged to create a final mouse brain template. Each original 3D-reconstructed brain was then spatially normalized to the template. Normalized brains were smoothed with a Gaussian kernel (full width at half maximum = $3 \times$ voxel dimension in the coronal plane). Voxels for each brain failing to reach a specified threshold in optical density (70% of the mean voxel value) were masked out to eliminate the background and ventricular spaces without masking grey or white matter. Differences in the absolute amount of radiotracer uptake in the brain were normalized in SPM for each mouse by scaling the voxel optical densities such that the whole-brain mean for each brain was the same (proportional scaling). For each condition (open-field and home cage exposure), one-tailed *t*-tests were performed voxel-by-voxel comparing 4EP⁺ and 4EP⁻ mice. The threshold for significance was set at $P < 0.05$ at the voxel level and an extent threshold of 200 contiguous voxels to eliminate false-positive statistically significant results. Colour-coded functional overlays showing statistically significant changes in rCGU were displayed over coronal sections of the template brain in MRIcro (v.1.40, <https://people.cas.sc.edu/orden/micro/micro.html>). This combination reflected a balanced approach to control both type I and type II errors. The minimum cluster criterion was applied to avoid basing our results on significance at a single or small number of suprathreshold voxels. Brain regions were identified according to a mouse brain atlas (ref. ⁴³ and <https://atlas.brain-map.org>).

A seed correlation approach was applied to assess 4EP-related differences in the functional connectivity of the PVT. A structural region of interest (ROI) was hand drawn in MRIcro over the template brain according to the mouse brain atlas for the PVT between bregma -1.0 mm and -1.6 mm . The mean optical density of the seed ROI was extracted for each mouse using the MarsBaR toolbox for SPM (v.0.42, <http://marsbar.sourceforge.net>). Correlation analysis was performed in SPM for each home cage group. *t* statistics were calculated using a linear regression model with the seed value as the only covariate (regressor). The threshold for significance of directional correlation was set at $P < 0.05$ (one-tailed *t*-test) at the voxel level and an extent threshold of 200 contiguous voxels to serve as a proxy for multiple comparison correction, which is standard for the field. Regions showing statistically significant correlations (positive or negative) in rCGU with the seed are considered to be functionally connected with the seed. Colour-coded functional overlays were displayed in the template brain after 3D rendering in MRIcro to enable a visual comparison of the overall level of functional connectivity.

Brain sample collection for immunohistochemistry analysis

Mice were perfused through the cardiovascular system with PBS followed by 4% paraformaldehyde (Electron Microscopy Sciences). Brains were removed and post-fixed in 4% paraformaldehyde for 1 day at 4°C . The brains were kept in PBS with 0.02% sodium azide at 4°C until sectioning. For sectioning, the brains were embedded in 4% UltraPure low melting point agarose (Thermo Fisher Scientific) and were coronally sectioned by vibratome (VT1000S; Leica Microsystems) at a thickness of $50 \mu\text{m}$. Brain sections of $50 \mu\text{m}$ were collected and stained every 0.15 mm . The brain sections were stored as free-floating in PBS with 0.02% sodium azide at 4°C until staining.

The free-floating sections were incubated with primary antibodies in blocking solution (10% horse serum, 0.3% Triton X-100 and 0.02% sodium azide in PBS) overnight at room temperature. The next day, sections were incubated with fluorescence-conjugated secondary antibodies for 1.5–2 h at room temperature. Between each step and after secondary antibody staining, sections were thoroughly washed with PBS or PBS with 0.1% Triton X-100 at least three times for 10 min each. The stained free-floating sections were then mounted onto the Superfrost Plus microscope slides (Thermo Fisher Scientific) in PBS. Excess PBS from adhered sections was carefully removed. Slides were dried at room temperature for 2–5 min. Then, 150–200 μl of ProLong Diamond, anti-fade mountant with DAPI (Thermo Fisher Scientific) was applied to the slides before placing the coverslip. The slides were left to set overnight before imaging.

The primary antibodies used for imaging throughout and their dilutions were as follows: mouse anti-NeuN (1:1,000; MAB377; Millipore Sigma), goat anti-Olig2 (1:500; AF2418; R&D Systems); mouse anti-CC1 (1:250; NB600-1021; Novus Biologicals); rabbit anti-NG2 (1:300; AB5320; Millipore Sigma); chicken anti-MBP (1:250; CH22112; Neuromics); mouse anti-neurofilament (1:250; 837802; BioLegend), rabbit anti-PLP (ab183493, Abcam). The fluorescent-conjugated secondary antibodies were donkey anti-goat (1:1,000; A-32814, A-21082, A11057; Thermo Fisher Scientific), donkey anti-rabbit (1:1,000; A-21206, A-10042, A-31573; Thermo Fisher Scientific), donkey anti-mouse (1:1,000; A-21202, A-10037, A-31571; Thermo Fisher Scientific) and donkey anti-chicken (1:1,000; A-11041; A-11039; A-21449, Thermo Fisher Scientific).

Microscopy imaging and image analysis

Imaging was performed using the Zeiss LSM 800 inverted confocal laser scanning microscope (Carl Zeiss) using Zen software (Carl Zeiss). Confocal images were obtained by z-stacks covering the entire z-axis range of the sections. The interval for each focal plane was $2 \mu\text{m}$ intervals. The images were then projected in the visualization plane with maximum intensity voxels (3D pixel) by maximum intensity projection using Zen software. Positively stained cells were quantified using a manual cell counter in ImageJ software (NIH). All of the images were minimally processed with brightness and contrast adjustment. The adjustment was applied equally across the entire image and consistent in the corresponding controls. Regions of interest were selected by a segmented line based on the anatomical features of each region. The final number of positive cells reported is averaged from four images.

The coordinates for imaging relative to bregma (bilateral) were: BLA: -1.06 to -2.06 mm ; BNST: $+0.38$ to $+0.26 \text{ mm}$; PVN and AH: -0.70 to -0.94 mm ; mPFC: $+1.10 \text{ mm}$; PVT: -0.70 to -1.58 mm ; LHB and MBH: -1.06 to -1.34 mm ; SM: -0.46 to -1.34 mm ; ACA: 0.26 mm ; CC: 0.26 mm ; LS and MS: 0.26 mm ; ME: -0.82 mm .

QuantSeq

After cervical dislocation, brains were extracted and placed in iced PBS for 5 min. The brains were placed upside down into a brain matrix (SA-2175, Roboz,) and sliced by single-edge blades (Personna). Brain slices were left on the blades and placed on ice to maintain RNA integrity. Specific brain regions were isolated by gross dissection or brain punches by using 1.0 mM Biopsy Punches (Miltex, VWR) and were immediately frozen in RNAlater (Qiagen) until RNA collection was performed according to the manufacturer’s recommendations using the Split RNA extraction kit (Lexogen).

Coordinates for mPFC brain slices spanned from anterior to posterior (AP) $+1.94 \text{ mm}$ to $+1.10 \text{ mm}$ relative to bregma. The gross anatomy of the mPFC was based on the morphology of corpus callosum and the appearance of lateral septum. Coordinates for BNST brain slices spanned from anterior to posterior (AP) $+0.62 \text{ mm}$ to $+0.14 \text{ mm}$ relative to bregma (bilateral). The gross anatomy of the BNST was based on the features of caudate putamen, lateral ventricle and anterior commissure.

Article

Coordinates for PVT brain slices spanned from anterior to posterior (AP) -0.94 mm to -1.58 mm relative to bregma. The gross anatomy of the PVT was based on the appearance of dorsal hippocampus. Coordinates for the hypothalamus spanned from anterior to posterior (AP) -0.58 mm to -2.92 mm relative to bregma. The gross anatomy of the hypothalamus was based on the medioventral part of the brain and covered numerous hypothalamic subregions. Coordinates for BLA brain slices spanned from anterior to posterior (AP) -1.06 mm to -2.06 mm relative to bregma (bilateral). The gross anatomy of the BLA was based on the terminal of external capsule branches nearby the piriform cortex. Coordinates for ventral hippocampus brain slices spanned from anterior to posterior (AP) -2.06 mm to -4.04 mm relative to bregma (bilateral). All coordinates and diagrams were based on the Paxinos and Franklin atlas⁴³.

Isolated brain tissue was immediately frozen in RNAlater (Qiagen) until RNA collection according to the manufacturer's recommendations using the Split RNA extraction kit (Lexogen). Quality control, library preparation and sequencing were performed by the Penn State College of Medicine's genome sciences facility as follows. The cDNA libraries were prepared using the QuantSeq 3'mRNA-Seq Library Prep Kit FWD for Illumina (Lexogen) according to the manufacturer's instructions. In brief, total RNA was reverse transcribed using oligo(dT) primers. The second cDNA strand was synthesized by random priming, in a manner in which DNA polymerase is efficiently stopped when reaching the next hybridized random primer, so only the fragment closest to the 3' end gets captured for later indexed adapter ligation and PCR amplification. The processed libraries were assessed for their size distribution and concentration using the BioAnalyzer High Sensitivity DNA Kit (Agilent Technologies, 5067-4626 and -4627). Pooled libraries were diluted to 2 nM in EB buffer (Qiagen, 19086) and then denatured using the Illumina protocol. The denatured libraries were pooled and diluted to 2 nM using 10 mM Tris-HCl, pH 8.5 and then denatured using the Illumina protocol. The denatured libraries were diluted to 10 pM by prechilled hybridization buffer and loaded a TruSeq SR v3 flow cell on an Illumina HiSeq 2500 system and run for 50 cycles using a single-read recipe according to the manufacturer's instructions. Single-end 50 bp reads were obtained. Demultiplexed sequencing reads were generated using Illumina bcl2fastq (v.2.18.0.12).

After quality and polyA trimming by BBduk (v.37.90; <http://jgi.doe.gov/data-and-tools/bb-tools/>) and alignment by STAR (v.2.5.2b)⁶², read counts were calculated from BAM files using Salmon (v.0.7.2)⁶³. The Ensembl genome was used with GENCODE annotation (GRCm38, M11). Quality statistics were also gathered from genome-aligned BAM files using Picard (v.2.5.0) to use in downstream differential gene expression analysis. Genes were filtered such that only genes with a counts per million (CPM) of >0.1 in at least 10% of samples were retained. Normalized expression data were obtained by taking $\log_2[CPM + 0.001]$. Then, 6 outliers were removed such that 114 samples were carried forward for differential gene expression analysis. Two of these outliers contained less than 1 million reads, and four samples were removed on the basis of the principal components plot of the normalized expression data (these samples did not cluster with other samples from the same brain region).

A linear regression was then conducted to test for differential gene expression in four groups (4EP⁺ post-EPM, 4EP⁺ baseline, 4EP⁻ post-EPM, 4EP⁻ baseline) separately within each brain region. The first five sequencing principal components (derived from the Picard sequencing statistics) were used as covariates in the linear regression to account for technical effects in the gene expression data. A one-way ANOVA test was then used to identify genes with any difference across our four test groups. This was followed by a post-hoc Tukey HSD test, which was performed on the genes with a significant false-discovery-rate-adjusted *P* value of less than 0.05 for the group ANOVA. Three specific comparisons were then made with the groups using the significantly differentially expressed genes from the post-hoc Tukey test (*P* < 0.05): (1) 4EP differences in the post-EPM, but not in homecage, baseline condition. (2) 4EP

differences at the baseline, but not in the post-EPM. (3) Baseline and post-EPM differences with 4EP. To gain a functional understanding of the genes in these comparisons, cell-type enrichment was performed using the pSI package⁶⁴ in R using cell type markers from Zhang et al.⁶⁵, and GO enrichment was performed using Go-Elite⁶⁶ and Metascape (<https://metascape.org>).

For visualization of the normalized gene expression data without the influence of technical factors, the effects of the five sequencing principal components were removed with a linear regression, such that only the model intercept, residual, behaviour, metabolite and regional gene expression effects remained. This regressed dataset was used to generate principal components for sample visualization. Metascape (<https://metascape.org>) was used to determine enriched GO terms in brain regions with sufficient differentially regulated genes, with *P* < 0.01 and biological processes as output.

Flow cytometry

Spleens or brain tissue dissections of the PVT, hypothalamus, cerebellum or cortex were collected. Single-cell suspensions were generated by passing the tissue through a 100 µm cell strainer (Corning) with syringe plunger and rinsed with HBSS (Corning) containing 10% FBS (Gibco, Life Technologies, Thermo Fisher Scientific). Red blood cell lysis was performed (Sigma-Aldrich), diluted with HBSS 10% FBS and the tissue suspension was centrifuged at 350g for 5 min at 4 °C. For brain regions, papain digestion in 1 ml (200 U papain, 0.1 mg ml⁻¹ DNase I) was performed for 20 min at 37 °C, samples were triturated gently through a 1,000 µl pipette tip, and then passed through a 40 µm filter. The samples were then mixed with 5–10 ml of 25% percoll in HBSS and centrifuged at 1,000g for 25 min in a swinging rotor. The myelin debris layer was aspirated from the top, the cell pellet was washed in HBSS 10% FBS and then resuspended in HBSS buffer containing Fc block (anti-Mo CD16/CD32, Ebioscience; Invitrogen) for 20 min at 4 °C. Further staining was performed as previously described for flow cytometry. Primary stains and antibodies included: aqua dead cell stain (Thermo Fisher Scientific) and anti-NG2 (1:400; Alexa488; Ebioscience), anti-MOG (1:100; biotinylated, Novus Biologicals), anti-CX3Cr1 (1:500, PE-Cy7, BioLegend), anti-CD45.2 (1:500, PerCP-Cy5.5, Tonbo), anti-CD11b (1:500, PE, BioLegend), anti-CD19 (1:500, FITC, BioLegend), anti-CD3e (1:500, PE, Thermo Fisher Scientific), anti-CD4 (1:500, APC, BioLegend), anti-TCRb (1:500, PerCP-Cy5.5, Tonbo), anti-CD8a (1:500, APC-Cy7, Thermo Fisher Scientific) antibodies, incubated with cells for 30 min at 4 °C. After washing, secondary streptavidin antibodies (1:1,000, SAV Alexa 647, 405237, BioLegend), was incubated with cells for 30 min at 4 °C. After washing, cells were fixed with 2% PFA for 20 min, washed and analysed on a 4 laser (Violet, Blue, Yellow and Red) CytoFLEX S Flow Cytometer in the Caltech Flow Cytometry Core Facility and analysed in Flowjo v.10.6.2.

MRI mouse brain scanning and data analysis

Brain samples were collected by cardiac perfusion as described above for immunohistochemistry analysis. Intact, defleshed skulls were collected and fixed in 4% PFA overnight, followed by incubation for 14 days at 4 °C in gadoteridol (Prohance, Bracco Diagnostics) and 0.01% sodium azide in PBS as previously described⁶⁷. The samples were scanned immersed in Krytox perfluoropolymer vacuum oil (Sigma-Aldrich), supported by cotton wool, in 15 ml conical tubes.

All MRI scans were performed using a Bruker Avance Neo 7T/30 scanner and a Bruker gradient and shim unit (B-GA12SHP insert for BGA20) supported by the Bruker PV360 software package. A Bruker quadrature volume coil (B-GA12s HP) and a mouse brain 2 × 2 receive-only four element array coil were used for ¹H RF pulse transmission and signal receiving, respectively, at its operating frequency of 300.33 MHz. A Bruker standard DWSE (diffusion weighted spin echo) sequence was used to collect images with a *b* value of 4,000 s mm⁻², gradient duration = 5.6 ms, gradient separation = 12.54 ms, repetition time

$TR = 200$ ms, echo time $TE = 23.34$ ms and using 60 gradient different directions. T_1 and T_2 weighted images were also collected using standard Bruker sequences (T1_FLASH_3D, T2_TurboRARE). Image resolution was fixed for all scanning at a field of view (FoV) = 14 mm and a resolution of 175 μm at each dimension. All GQI-based tractographic images were acquired after data analysis that was performed using the DSI Studio software package⁶⁸. The total surface area (TSA), dfl_FA, MD, AD and RD of tracts were calculated using built-in functions of the DSI studio after individual ROI (that is, PVT) was first calculated using the implemented routine under CIVM mouse atlas (Duke radiology, <https://www.civm.duhs.duke.edu/>). The GQI-based diffusion data reconstruction was performed with a diffusion sampling length ratio of 1.2. A deterministic fibre tracking algorithm was used⁶⁹. In track calculations, a seeding region was placed at whole brain and the change threshold was set to 20% uniformly and the angular threshold was randomly selected. The tracking anisotropy threshold was varied from 0.06–0.1, depending on the ROIs used (Extended Data Fig. 7). The step size was randomly selected from 0.5 voxels to 1.5 voxels. Various minimum and maximum track lengths were tested, but we have not seen any significant difference among track parameter values, and data reported here are limited for tracks within the 5 mm < L < 10 mm range. A total of 20,000 tracts were calculated.

Electron microscopy analysis

Mice were anesthetized using 150 μl Euthasol and perfused with 30 ml of 37 °C PBS followed by 40–50 ml 37 °C 4% PFA at 6 ml min^{-1} flow rate. Brains and intestinal tissue were collected and continuously hydrated with cold (4 °C) fixative solution of 3% glutaraldehyde, 1% paraformaldehyde, 5% sucrose in 0.1 M sodium cacodylate trihydrate throughout the dissection process. Fixed brains were rapidly dissected out and fitted into 1.0 mm brain matrix (Roboz, SA-2175) where two gross cuts were made at +0.75 mm and –0.25 mm relative to bregma. Brain tissue anterior to +0.75 mm and posterior to –0.25 mm was discarded. The remaining tissue block was cut at positions ± 0.5 mm lateral to the midline and the flanking tissues were discarded. The remaining tissue dorsal and ventral to the visible corpus callosum was excised and discarded. Fixed intestines were rapidly dissected out and cuts were made to collect the proximal colon. The 2 mm^3 of intestinal tissue or 1 mm^3 brain tissue containing the corpus callosum were immediately stored in the cold fixative solution until proceeding to the next step.

Corpus callosum tissue was placed into Petri dishes with 0.1 M cacodylate buffer and cut into $\sim 1 \text{ mm}^2 \times 0.5 \text{ mm}$ thick slices using a microsurgical scalpel. These were placed individually into brass high-pressure freezing planchettes (Ted Pella) with cacodylate buffer containing 10% Ficoll (an extracellular cryoprotectant). The samples were ultra-rapidly frozen with an HPM-010 high-pressure freezing machine and transferred to liquid nitrogen. Planchettes containing vitrified tissue were transferred under liquid nitrogen to cryotubes (Nunc) prefilled with 2% OsO₄ and 0.05% uranyl acetate in acetone. The samples were placed in a AFS-2 freeze-substitution machine (Leica Microsystems), processed at –90 °C for 72 h, warmed to –20 °C over 12 h, further processed at that temperature for 24 h, and then rinsed with acetone and flat-embedded in Epon-Araldite resin (Electron Microscopy Sciences) between Teflon-coated glass slides. Resin was polymerized at 60 °C for 48 h.

Embedded tissue blocks were observed by phase-contrast microscopy to select well-preserved and optimally oriented regions, then extracted with a scalpel and glued to plastic sectioning stubs. Semi-thick (300–400 nm) serial sections were cut with an EM UC-6 ultramicrotome (Leica Microsystems) using a diamond knife (Diatome US). The sections were collected onto Formvar-coated copper/rhodium slot grids and stained with 3% uranyl acetate and lead citrate. Colloidal gold particles (10 nm) were placed onto both surfaces of the grids to serve as fiducial markers for tomographic image alignment.

Tomography

Grids were placed in a dual-axis tomography holder (Model 2040, E.A. Fischione Instruments) and imaged with a TF-30ST transmission electron microscope (Thermo Fisher Scientific) at 300 KeV. For tomography, grids were tilted $\pm 64^\circ$ and images acquired at 1° increments. The grid was then rotated 90° and a similar tilt-series was taken about the orthogonal axis. Tilt-series were acquired automatically using the SerialEM software package⁶⁸ and recorded with a CCD camera (US1000, Gatan). Tomographic datasets were processed and analysed using the IMOD software package^{70,71} on MacPro and iMacPro computers (Apple).

Western blot analysis

Western blots were performed on the PVT using brain punches that were collected using 1.0 mM Biopsy Punches (Miltex, VWR), or on ex vivo organotypic brain slices. The tissue samples were homogenized by bead beating in lysing matrix D tubes (MP Biomedicals) in RIPA buffer (Millipore Sigma) containing Protease Inhibitor tablets (Roche) followed by protein quantification and normalization using the Pierce BCA Protein Assay Kit (Thermo Fisher Scientific). Proteins were separated by SDS page using 4–20% tris-glycine Wedgewell gels (Invitrogen) and blotted onto a 0.45 μm PVDF membrane (Millipore Sigma). β -Actin loading controls were used, and images were taken of the same blot under specific excitation wavelengths for the various protein visualization. Antibody titrations were 1:500 for primary antibodies and 1:5,000 for fluorescent-conjugated secondary antibodies. Antibodies included: mouse anti-MOG (CL2858, Thermo Fisher Scientific), chicken anti-MBP (CH22112, Neuromics), rabbit anti- β -actin (13E5, Cell Signaling), secondary anti-chicken-488 (ab150173, Abcam), secondary anti-mouse-488 (ab150113, Abcam) and secondary anti-rabbit-647 (A31573, Thermo Fisher Scientific) antibodies.

Organotypic brain slice culturing

Brains from P8 mice were sectioned by Vibratome into 300 μm sections in HBSS with 3 mM HEPES while bubbling in carbogen gas. Sections were cultured at 37 °C with 5% CO₂ on 12-well Transwell membrane plates in 50% DMEM/HEPES (Gibco) containing 25% heat-inactivated horse serum (Gibco), 25% Hank's solution (Gibco), 2 mM sodium bicarbonate (Merck), 6.5 mg ml^{-1} glucose, 2 mM glutamine, 1× penicillin–streptomycin (Gibco), pH 7.2. The samples were visually observed for general signs of health (adherence, spread on membrane) and viability tested by standard lactate dehydrogenase and alamarblue assays as previously described⁷². After 10 days culture in the presence of 10 μM 4EPS or vehicle (PBS), the samples were taken for downstream western blot and qPCR as described above. For immunohistochemistry, the samples were fixed in 4% paraformaldehyde for 3 h at 4 °C and stained for neurofilament and PLP as described above. Colocalization was quantified using IMARIS software.

Analysis of myelination and calculation of g-ratio

Tomograms containing cross-sectional images of myelinated and unmyelinated axons were visualized in 3D using IMOD and analysed using the 3dmod image-processing program. Myelinated and unmyelinated axons were differentiated by eye and counted accordingly. To calculate the g-ratio (ratio of axon radius to its outer, myelinated radius), the edge of the axon and the edge of the outer myelin sheath were traced using the Object tool. Traces were analysed for area, yielding one inner and one outer area per myelinated axon. Radii were determined using the formula $r_{\text{axon}} = \sqrt{(A_{\text{axon}}/\pi)}$ for the bare axon, and $r_{\text{axon+myelin}} = \sqrt{(A_{\text{axon+myelin}}/\pi)}$ for the myelinated axon. Final g-ratios were calculated as $r_{\text{axon}}/r_{\text{axon+myelin}}$. Every axon apparent in the tomogram was included in all analyses of myelination.

Behaviour testing

Behaviour testing was performed as previously described^{8,51,73–77}. All of the mice were tested by a researcher in a blinded manner starting at six

Article

weeks of age, in the following order: EPM, light/dark box, open-field testing, marble burying, grooming, social behaviour and ultrasonic vocalization (male–female context). Separate cohorts of mice were used to test cognitive and motor function. These cohorts were tested in EPM to confirm phenotype followed by novel object recognition and Y-maze or beam traversal, pole descent and wire hang. Mice were allowed to settle for at least 2 days after cage changing before they were tested, and tests were performed 2–3 days apart to enable the mice to rest between tests. The mice were acclimatized to the behaviour-testing room for 1 h before testing. Mice were tested during the light phase of the light cycle.

EPM

EPM was performed in a maze with 25 cm by 5 cm arms and a 5 cm by 5 cm centre, recorded using an overhead camera, and tracked and analysed using the EthoVision XT 4 software package (Noldus Information Technology). Before testing, the maze was disinfected using Rescue disinfectant (Virox technologies) and then allowed to evaporate. Mice were then introduced to the arena and allowed to explore for 5 min while being tracked. The number of entries into and the time spent in open and closed arms as well as the outer third of the open arms (the terminus) were analysed. If a mouse fell or jumped from the apparatus during the test it was removed from the dataset.

Light/dark box

The light/dark box test was performed in a $50 \times 30 \text{ cm}^2$ arena with a $30 \times 30 \text{ cm}^2$ open section and a black, lidded section sized $20 \times 30 \text{ cm}^2$ with an open doorway for free passage from light to dark areas. Before testing, the arena was disinfected using Rescue disinfectant (Virox technologies), which was then allowed to evaporate. Mice were placed into the dark box and the lid was replaced, and the mice were then recorded using an overhead camera, and tracked and analysed using the EthoVision XT 10 software package (Noldus Information Technology). Entry and duration in the light was analysed over a 10 min period.

Open-field test

The open-field test was performed in $50 \times 50 \text{ cm}^2$ white Plexiglas arenas, recorded using an overhead camera, and tracked and analysed using the EthoVision XT 4 software package (Noldus Information Technology). Before testing, the arena was disinfected using Rescue disinfectant (Virox technologies), which was then allowed to evaporate. The mice were then introduced to the arena and allowed to explore for 10 min while being tracked. The total distance travelled, and the number of entries and time spent in a $17 \times 17 \text{ cm}^2$ centre square were analysed. Faecal pellets left during the assay were quantified.

Marble burying

Marble burying was performed in a normal cage bottom (Lab Products) filled with 3–4 cm of fresh, autoclaved wood chip bedding (Aspen chip bedding, Northeastern Products). The mice were first habituated to the cage for 10 min, and subsequently transferred to a holding cage while the bedding was levelled and 20 glass marbles (4×5) were placed on top. The mice were then returned to their own cage and removed after 10 min. The number of buried marbles (50% or more covered) was then recorded and photographed for reference and scored by an additional blinded researcher. A fresh cage was used for each mouse, and marbles were soaked in Rescue Disinfectant (Virox Technologies) and dried in bedding in between tests.

Grooming

Mice were placed in autoclaved, empty standard cages (Lab Products) and video recorded from the side for 15 min. The final 10 min were scored manually by two independent blinded, trained researchers for grooming behaviour.

Social interaction

Each mouse was introduced to a fresh, empty, standard, autoclaved cage (Lab Products) and allowed to habituate for 10 min before a novel mouse matched in age and sex was introduced to the cage for an additional 5 min for scoring of social activity. Two blinded, trained researchers scored videos for any social behaviour using the ETHOM software⁷⁸.

Ultrasonic vocalization

Mice were single-housed and exposed to a new SPF C57BL/6J female for 10 min every day in the 5 days before the test. On the fourth day, mice were habituated to an empty cage (with no bedding) with a filter soaked with 10 µl of fresh pooled female urine for 10 min. Subsequently, a new female mouse was introduced to the cage and ultrasonic vocalizations were recorded using Avisoft UltraSoundGate 116Hme microphone (Avisoft Bioacoustics) and the Avisoft Sas-lab Recorder software (Avisoft Bioacoustics). Total vocalization and vocalization counts were recorded during 3 min sessions of male–female interaction.

Novel object recognition

Novel object recognition was performed as described previously with sand-filled flasks and Duplo towers⁷³. Mice were habituated to the open-field arenas ($50 \times 50 \text{ cm}^2$ white Plexiglass) for 10 min on day 1. On day 2, the mice were reintroduced to the arena with duplicate-copies of one of two objects. On day 3, the mice were reintroduced to the arena with one copy of the familiar object and one copy of a novel object. Within each group of mice, the mice were split such that both objects were used as the familiar object to control for inherent interest levels in the different objects. Time spent with the nose cone directed toward the objects and within 2 cm from the objects was scored using the EthoVision XT 10 software package (Noldus Information Technology). The novel object recognition index was calculated as the time at novel object/total time at objects × 100.

Y maze

The Y-maze alternations test was performed in a white Y maze (Maze Engineers), video-taped from above. Entries into each arm were scored manually by a blinded researcher and the number of repetitive, spontaneous alternations were calculated.

Beam traversal

Beam traversal was performed as previously described⁷⁴ on a 1 m plexiglass beam (Stark's Plastics) constructed of four segments of 0.25 m length, with each segment decreasing in widths from 3.5 cm, 2.5 cm, 1.5 cm and 0.5 cm, with 1cm overhangs placed 1 cm below the surface of the beam. The widest segment acted as a loading platform for the mice and the narrowest end placed into home cage. The mice had 2 days of training to traverse the length of the beam before testing. On the first day of training, the mice received one trial with the home cage positioned close to the loading platform and guided the mice forwards along the narrowing beam. The mice received two more trials with limited or no assistance to encourage forward movement and stability on the beam. On the second day of training, the mice had three trials to traverse the beam and generally did not require assistance in forward movement. On the third day, the mice were timed using a stopwatch to traverse from the loading platform and to the home cage. Timing began when the mice placed their forelimbs onto the 2.5 cm segment and ended when one forelimb reached the home cage.

Pole descent

Pole descent was performed as previously described⁷⁴ with a 0.5 m long pole, 1 cm in diameter, wrapped with non-adhesive shelf liner to facilitate the grip of the mice, which were placed into the home cage. The mice received 2 days of training to descend from the top of the pole and into the home cage. On day one of training, the mice received three trials. For the

first trial, the animals were placed head-down 1/3 of the distance above the floor; for the second trial, the mice were placed 2/3 of the distance above the floor; and, for the third trial, the mice were placed at the top. On the second day of training, the mice were given three trials to descend, head-down, from the top of the pole. On the test day, the animals were placed head-down on the top of the pole and timed to descend back into the home cage. Timing began when the experimenter released the mouse and ended when one hindlimb reached the home cage base.

Wire hang

Wire hang was performed as previously described⁷⁴. The mice were placed in the centre of a 30 × 30 cm² screen with a 1-cm-wide mesh. The screen was inverted head-over-tail and placed on supports ~40 cm above an open, clean cage with bedding. Mice were timed until they released their grip or remained for 60 s.

Statistical information

All data are represented as mean ± s.e.m. Two-tailed unpaired Welch's *t*-tests were used to compare data between two independent groups (that is, 4EP[−] versus 4EP⁺). Data with more than two independent groups were analysed using one-way ANOVA with Dunnett's multiple-comparison correction or Sidak multiple-comparison correction, according to specific experimental design. All data were analysed using GraphPad Prism; a *P* value (or adjusted *P* value in the case of ANOVA with multiple-comparison correction) of less than 0.05 was deemed to be statistically significant. The number of biological replicates is indicated in all of the figures and the statistical methods are noted in the figure legends and Methods. The number of asterisks indicates the difference in the figures, with exact *P* values in the legends. For comprehensive statistical information regarding the autoradiography, fUSi and QuantSeq experiments, see the corresponding detailed paragraphs above.

Reporting summary

Further information on research design is available in the Nature Research Reporting Summary linked to this paper.

Data availability

All data analysed for this study are included in this published Article and its Supplementary Information. Additional 2DG data are available online (https://gin.g-node.org/bneedham/Needham_Nature_2022). The WoL database annotation files are publicly available at GitHub (<https://biocore.github.io/wol/download>). The Greengenes database is publicly available online (<https://greengenes.secondgenome.com/>). Source data are provided with this paper.

Code availability

Custom scripts used in the fUSi analysis are available at GitHub (https://github.com/brittanyneedham/Needham_Nature2022).

44. Holdeman, L. V. & Moore, W. E. C. *Anaerobe Laboratory Manual* 4th edn (Virginia Polytechnic Institute and State University, 1977).
45. Martens, E. C., Chiang, H. C. & Gordon, J. I. Mucosal glycan foraging enhances fitness and transmission of a saccharolytic human gut bacterial symbiont. *Cell Host Microbe* **4**, 447–457 (2008).
46. Koropatkin, N. M., Martens, E. C., Gordon, J. I. & Smith, T. J. Starch catabolism by a prominent human gut symbiont is directed by the recognition of amylose helices. *Structure* **16**, 1105–1115 (2008).
47. Bolyen, E. et al. Reproducible, interactive, scalable and extensible microbiome data science using QIIME 2. *Nat. Biotechnol.* **37**, 852–857 (2019).
48. Callahan, B. J. et al. DADA2: high-resolution sample inference from Illumina amplicon data. *Nat. Methods* **13**, 581–583 (2016).
49. Banoglu, E. & King, R. S. Sulfation of indoxyl by human and rat aryl (phenol) sulfotransferases to form indoxyl sulfate. *Eur. J. Drug Metab. Pharmacokinet.* **27**, 135–140 (2002).
50. Teubner, W., Meini, W., Florian, S., Kretzschmar, M. & Glatt, H. Identification and localization of soluble sulfotransferases in the human gastrointestinal tract. *Biochem. J.* **404**, 207–215 (2007).
51. Sharon, G. et al. Human gut microbiota from autism spectrum disorder promote behavioral symptoms in mice. *Cell* **177**, 1600–1618 (2019).
52. Iadecola, C. The neurovascular unit coming of age: a journey through neurovascular coupling in health and disease. *Neuron* **96**, 17–42 (2017).
53. Mace, E. et al. Functional ultrasound imaging of the brain: theory and basic principles. *IEEE Trans. Ultrason. Ferroelectr. Freq. Control* **60**, 492–506 (2013).
54. Tiran, E. et al. Transcranial functional ultrasound imaging in freely moving awake mice and anesthetized young rats without contrast agent. *Ultrasound Med. Biol.* **43**, 1679–1689 (2017).
55. Needham, B. D. et al. A gut-derived metabolite alters brain activity and anxiety behaviour in mice. GitHub https://github.com/brittanyneedham/Needham_Nature2022 (2022).
56. Demené, C. et al. Spatiotemporal clutter filtering of ultrafast ultrasound data highly increases doppler and fultrasound sensitivity. *IEEE Trans. Med. Imaging* **34**, 2271–2285 (2015).
57. Osmanski, B.-F., Pezet, S., Ricobaraza, A., Lenkei, Z. & Tanter, M. Functional ultrasound imaging of intrinsic connectivity in the living rat brain with high spatiotemporal resolution. *Nat. Commun.* **5**, 5023 (2014).
58. Armstrong, R. A. When to use the Bonferroni correction. *Ophthalmic Physiol. Opt.* **34**, 502–508 (2014).
59. Holschneider, D. P., Guo, Y., Wang, Z., Vidal, M. & Scrimin, O. U. Positive allosteric modulation of cholinergic receptors improves spatial learning after cortical contusion injury in mice. *J. Neurotrauma* **36**, 2233–2245 (2019).
60. Sokoloff, L. Localization of functional activity in the central nervous system by measurement of glucose utilization with radioactive deoxyglucose. *J. Cereb. Blood Flow Metab.* **1**, 7–36 (1981).
61. Wang, Z., Pang, R. D., Hernandez, M., Ocampo, M. A. & Holschneider, D. P. Anxiolytic-like effect of pregabalin on unconditioned fear in the rat: an autoradiographic brain perfusion mapping and functional connectivity study. *Neuroimage* **59**, 4168–4188 (2012).
62. Dobin, A. et al. STAR: ultrafast universal RNA-seq aligner. *Bioinformatics* **29**, 15–21 (2013).
63. Patro, R., Duggal, G., Love, M. I., Irizarry, R. A. & Kingsford, C. Salmon provides fast and bias-aware quantification of transcript expression. *Nat. Methods* **14**, 417–419 (2017).
64. Xu, X., Wells, A. B., O'Brien, D. R., Nehorai, A. & Dougherty, J. D. Cell type-specific expression analysis to identify putative cellular mechanisms for neurogenetic disorders. *J. Neurosci.* **34**, 1420–1431 (2014).
65. Zhang, Y. et al. An RNA-sequencing transcriptome and splicing database of glia, neurons, and vascular cells of the cerebral cortex. *J. Neurosci.* **34**, 11929–11947 (2014).
66. Zambon, A. C. et al. GO-Elite: a flexible solution for pathway and ontology over-representation. *Bioinformatics* **28**, 2209–2210 (2012).
67. Tyszk, J. M., Readhead, C., Bearer, E. L., Pautler, R. G. & Jacobs, R. E. Statistical diffusion tensor histology reveals regional dysmyelination effects in the shiverer mouse mutant. *Neuroimage* **29**, 1058–1065 (2006).
68. Mastronarde, D. N. Automated electron microscope tomography using robust prediction of specimen movements. *J. Struct. Biol.* **152**, 36–51 (2005).
69. Yeh, F.-C. et al. Deterministic diffusion fiber tracking improved by quantitative anisotropy. *PLoS ONE* **8**, e80713 (2013).
70. Kremer, J. R., Mastronarde, D. N. & McIntosh, J. R. Computer visualization of three-dimensional image data using IMOD. *J. Struct. Biol.* **116**, 71–76 (1996).
71. Mastronarde, D. N. Correction for non-perpendicularity of beam and tilt axis in tomographic reconstructions with the IMOD package. *J. Microsc.* **230**, 212–217 (2008).
72. Carranza-Torres, I. E. et al. Organotypic culture of breast tumor explants as a multicellular system for the screening of natural compounds with antineoplastic potential. *BioMed Res. Int.* **2015**, 618021 (2015).
73. Leger, M. et al. Object recognition test in mice. *Nat. Protoc.* **8**, 2531–2537 (2013).
74. Sampson, T. R. et al. Gut microbiota regulate motor deficits and neuroinflammation in a model of Parkinson's disease. *Cell* **167**, 1469–1480 (2016).
75. Komada, M., Takao, K. & Miyakawa, T. Elevated plus maze for mice. *J. Vis. Exp.* <https://doi.org/10.3791/1088> (2008).
76. Takao, K. & Miyakawa, T. Light/dark transition test for mice. *J. Vis. Exp.* <https://doi.org/10.3791/104> (2006).
77. Miedel, C. J., Patton, J. M., Miedel, A. N., Miedel, E. S. & Levenson, J. M. Assessment of spontaneous alternation, novel object recognition and limb clasping in transgenic mouse models of amyloid-β and Tau neuropathology. *J. Vis. Exp.* **28**, 55523 (2017).
78. Shih, H.-T. & Mok, H.-K. ETHOM: event-recording computer software for the study of animal behavior. *Acta Zool. Taiwanica* **11**, 47–61 (2000).

Acknowledgements We thank the members of the Mazmanian laboratory for evaluating the manuscript; S. Reisman and L. Chapman (Caltech) for synthesizing 4EPS; the staff at the Caltech Kavli Nanoscience Institute for help with maintaining the TF30 electron microscope, and the Gordon and Betty Moore and Beckman Foundations for gifts to Caltech to support electron microscopy. Funding: this work was supported by funds from the Center for Environmental Microbial Interactions to B.D.N., National Science Foundation MRI grant 1920364 for Bruker console upgrading, the Human Frontier Science Program (grant no. LT000217/2020-C) to C.R., the National Institutes of Health (NIH) (2 P50 GM082545-08) to P.J.B., the Ministry of Science and Technology in Taiwan (MOST107-2320-B-006-072-MY3; MOST108-2321-B-006-025-MY2) to W.-L.W., and the Heritage Medical Research Institute, L. and B. Fetter, and the NIH (MH100556 and AG063744) to S.K.M.

Author contributions Conceptualization: B.D.N. and S.K.M. Methodology: B.D.N., M.F., M.D.A., Z.W., W.-L.W., J.H., M.S.L., J.A.G., C.R., S.-J.H. and D.P.H. Formal analysis: B.D.N., M.D.A., Z.W. and J.H. Investigation: B.D.N., M.F., M.D.A., Z.W., W.-L.W., J.C.B., C.R., J.H., S.-J.H., Q.Z., M.S.L. and Y.G. Biochemical pathway investigation and strain engineering: M.F. and M.A.F. Gene abundance analysis: Q.Z., J.C.B. and R.K. fUSi imaging: C.R., J.C.B., B.D.N. and M.G.S. 2DG analysis: Z.W., B.D.N., Y.G. and D.P.H. QuantSeq analysis: J.H., W.-L.W., B.D.N. and D.H.G. Oligodendrocyte characterization: B.D.N., M.D.A., J.C.B., M.S.L. and J.A.G. ET: M.S.L., B.D.N. and M.D.A. MRI/diffusion tensor imaging: S.-J.H. and B.D.N. Animal behaviour: B.D.N. and M.D.A.

Article

Resources: P.J.B., D.G., D.P.H., M.A.F., R.K., M.G.S. and S.K.M. Writing original draft: B.D.N. Writing review and editing: B.D.N., M.F., M.D.A., Z.W., W.-L.W., J.H., M.S.L., J.A.G., D.P.H., M.A.F. and S.K.M. Visualization: B.D.N., M.F., M.D.A., Z.W., W.-L.W., J.H., J.C.B., C.R., S.-J.H., M.S.L. and M.A.F. Supervision: S.K.M. Project administration: B.D.N. Funding acquisition: B.D.N., W.-L.W., P.J.B. and S.K.M.

Competing interests S.K.M. has financial interests in Axial Biotherapeutics. The other authors declare no competing interests.

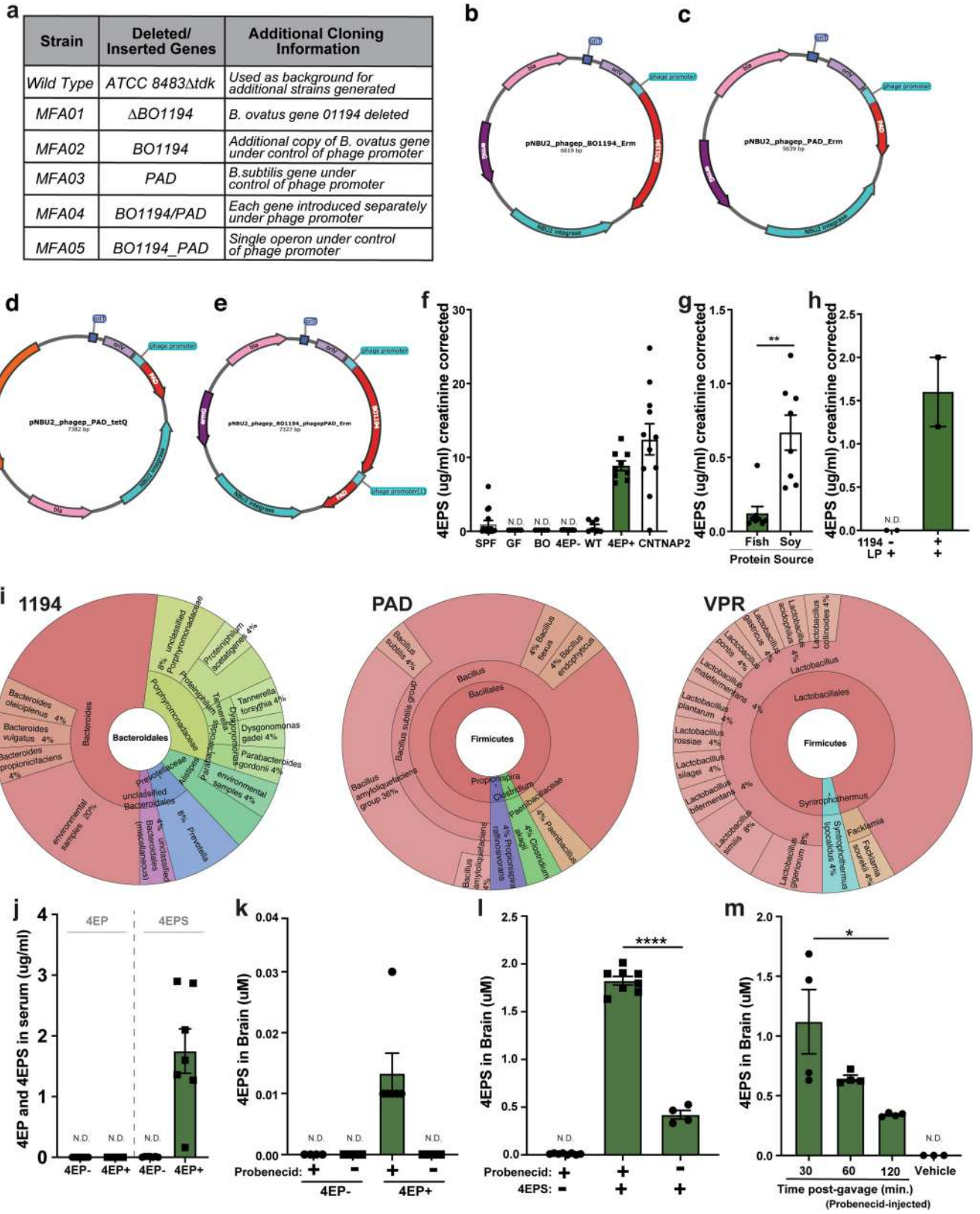
Additional information

Supplementary information The online version contains supplementary material available at <https://doi.org/10.1038/s41586-022-04396-8>.

Correspondence and requests for materials should be addressed to Brittany D. Needham or Sarkis K. Mazmanian.

Peer review information *Nature* thanks Gabriel Corfas, Jane Foster, Robert Quinn and the other, anonymous, reviewer(s) for their contribution to the peer review of this work.

Reprints and permissions information is available at <http://www.nature.com/reprints>.

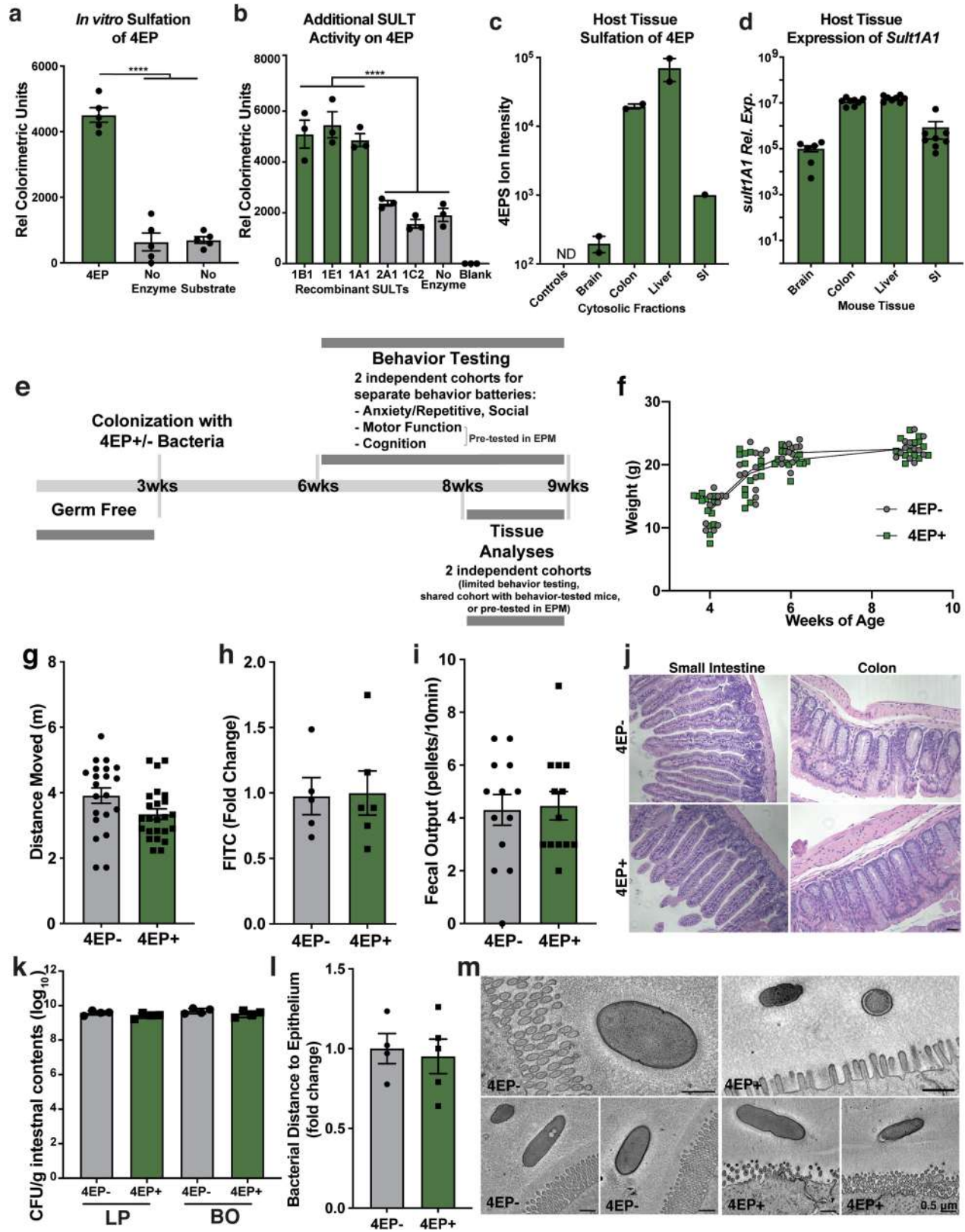


Extended Data Fig. 1 | See next page for caption.

Article

Extended Data Fig. 1 | Strain engineering and 4EPS quantification. **a**, Strain legend corresponding to Fig. 1b–d, containing further details for strain names and cloning strategy. Additional information can be found in the Methods and Supplementary Tables 1–3. **b–e**, Maps for integration vectors. **b**, The BO1194 gene was cloned into the pNBU2 vector with an erythromycin resistant marker under the phage promoter. **c**, The PAD gene was cloned into pNBU2 vector with an erythromycin resistant marker under the phage promoter. **d**, The PAD gene was cloned into the pNBU2 vector with a tetracycline resistant marker under the phage promoter. **e**, BO1194 and PAD were tandemly connected, putting the phage promoter in front of both genes, then cloned into the pNBU2 vector with the erythromycin resistant marker. **f**, Creatinine corrected urinary levels of 4EPS from SPF, GF, gnotobiotic mice colonized with strains as labelled, and a mouse model of atypical behaviour including anxiety-like phenotypes. This data corresponds to abbreviated data in Fig. 1f. SPF, specific pathogen free mice; BO, *Bacteroides ovatus* mono-colonized mice; 4EP⁺, GF mice colonized with non-producing strain pair (*B. ovatus* Δ1194 and WT *L. plantarum* with endogenous VPR) used throughout; WT, GF mice colonized with wild type strain pair (WT *B. ovatus* and WT *L. plantarum* with endogenous VPR) before optimal engineering; 4EP⁺, colonized with strain pair engineered for higher production of 4EP⁺ (*B. ovatus*+1194/PAD and WT *L. plantarum* with endogenous VPR), used throughout; CNTNAP2, conventionally colonized mouse model of atypical behaviour (left to right columns: n=15, 5, 5, 9, 7, 9, 11). **g**, 4EPS levels (creatinine corrected) in urine of wild type, specific pathogen free (SPF) mice fed one of two isocaloric diets matched for protein, mineral, carbohydrate, and

fat levels but differing in either high tyrosine fish meal (fish diet), or a high plant protein (soy diet) (n=8 each group) $p=0.002$. **h**, 4EPS levels (creatinine corrected) in urine of gnotobiotic mice colonized with isogenic strain pairs of *B. ovatus* and wild type *L. plantarum*, which differ only in the presence or absence of gene 1194, and thus the tyrosine lyase activity requires to convert tyrosine to p-coumaric acid (n=2 each group). **i**, Alignments of genes used to engineer the 4EP synthesis pathway to the reference genomes in the WoL database, showing that these genes are found in ~25 genomes each, most of which are common human gut lineages. **j**, 4EP and 4EPS levels (ug/ml) in serum of colonized mice (n=7 each group). **k**, 4EP⁺ and 4EP⁻ colonized mice were injected with the organic anion transporter to inhibit potential 4EPS transport out of the brain, then analysed by LCMS (n=6 each group). Extended Data Fig. 1g. **l**, Conventionally colonized (SPF) mice were injected with probenecid and then injected with high dose 4EPS (n=8) or saline vehicle (n=8), and whole brain lysate was analysed by LCMS compared to 4EPS injection alone (n=4) $p<0.0001$. **m**, Conventionally colonized (SPF) mice were injected with probenecid and then gavaged with 4EP, then whole brains were harvested at 30-minute intervals and 4EPS levels were quantified by LCMS (n=4; vehicle group n=3) $p=0.01$. Two independent trials on biological replicates were used for the experiments in the figure. Abbreviations: SPF, specific pathogen-free; GF, germ-free; BO, *Bacteroides ovatus*; WT, wild type; LP, *Lactobacillus plantarum*. Data represent mean ± SEM analysed by a two-tailed Welch's t-test or one-way ANOVA with Dunnett multiple comparisons test as appropriate. * $p\leq 0.05$; ** $p\leq 0.01$; *** $p\leq 0.001$; **** $p\leq 0.0001$.

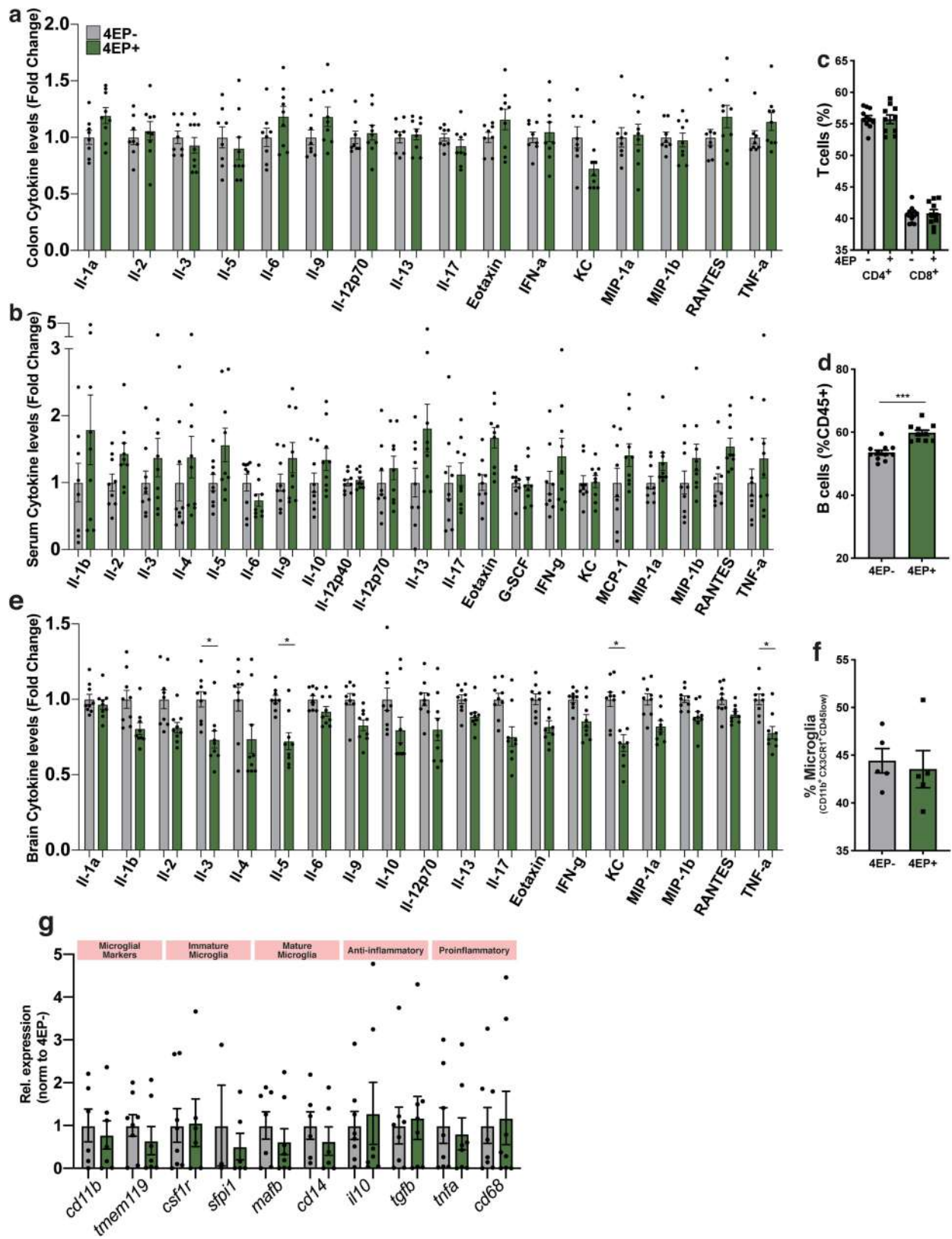


Extended Data Fig. 2 | See next page for caption.

Article

Extended Data Fig. 2 | 4EP sulfation, experimental timeline, normal weight gain, colonization and intestinal barrier of 4EP⁺ mice. **a**, In vitro recombinant SULT1A1 sulfotransferase assay with 4EP as potential sulfate acceptor (n=5) $p<0.0001$. **b**, Results of the sulfotransferase assay using various recombinant SULTs (n=3) $p<0.0001$. **c**, 4EP sulfation capacity of cytosolic fractions of brain, colon, liver, and small intestinal tissue, each containing endogenous sulfotransferases (n=2 datapoints of samples pooled from triplicate biological replicates, with only 1 pool for SI). Ion intensity of 4EPS measured by LCMS is plotted along the y-axis. **d**, Confirmation of expression of the *Sult1a1* gene measured by qPCR in tissue from the brain, colon, liver, and small intestine of colonized mice (n=8; brain n=6) $p<0.0001$. **e**, Schematic of mouse experimental timeline, showing ages of mice at colonization of GF mice with 4EP+/- strains, behaviour testing and tissue collection. **f**, Weights of mice (grams) after colonization of GF mice with 4EP⁻ or 4EP⁺ bacteria (n=13). **g**, Ambulatory activity of 4EP⁻ and 4EP⁺ mice over ten minutes, measured by distance moved when mice were placed in an open arena and allowed to explore (4EP⁻ n=21; 4EP⁺ n=24). **h**, FITC-dextran levels in

serum as a measure of intestinal permeability (4EP⁻ n=5, 4EP⁺ n=6). **i**, Faecal output of colonized mice over 10 min (n=13). **j**, Images of hematoxylin and eosin (H&E) stained small intestine and colon of 4EP+/- mice (representative images of n=4). Scale bar 50 μ m. **k**, Colonization of ex-GF mice with engineered *Bacteroides ovatus* (BO) and *Lactobacillus plantarum* (LP), plotted as colony forming units (CFU) per gram of intestinal contents (n=4). **l**, Quantification of bacterial distance from the intestinal epithelium imaged by electron tomography, where each data point represents a separate animal comprised of an average of 5-10 bacterial cells per image per mouse (4EP⁻ n=4; 4EP⁺ n=5). **m**, Example images of bacterial cells near the intestinal epithelial layer of 4EP+/- mice. Two independent trials using multiple randomized litters were used for the experiments in the figure. Abbreviations: SULT, sulfotransferase; SI, small intestine. Data represent mean \pm SEM. Panel f was analysed by a 2-way ANOVA with a Bonferroni multiple comparison correction. Panels g-i and l were analysed using two-tailed Welch's t-tests and panels a-d, k by a one-way ANOVA with Dunnett multiple comparisons test.

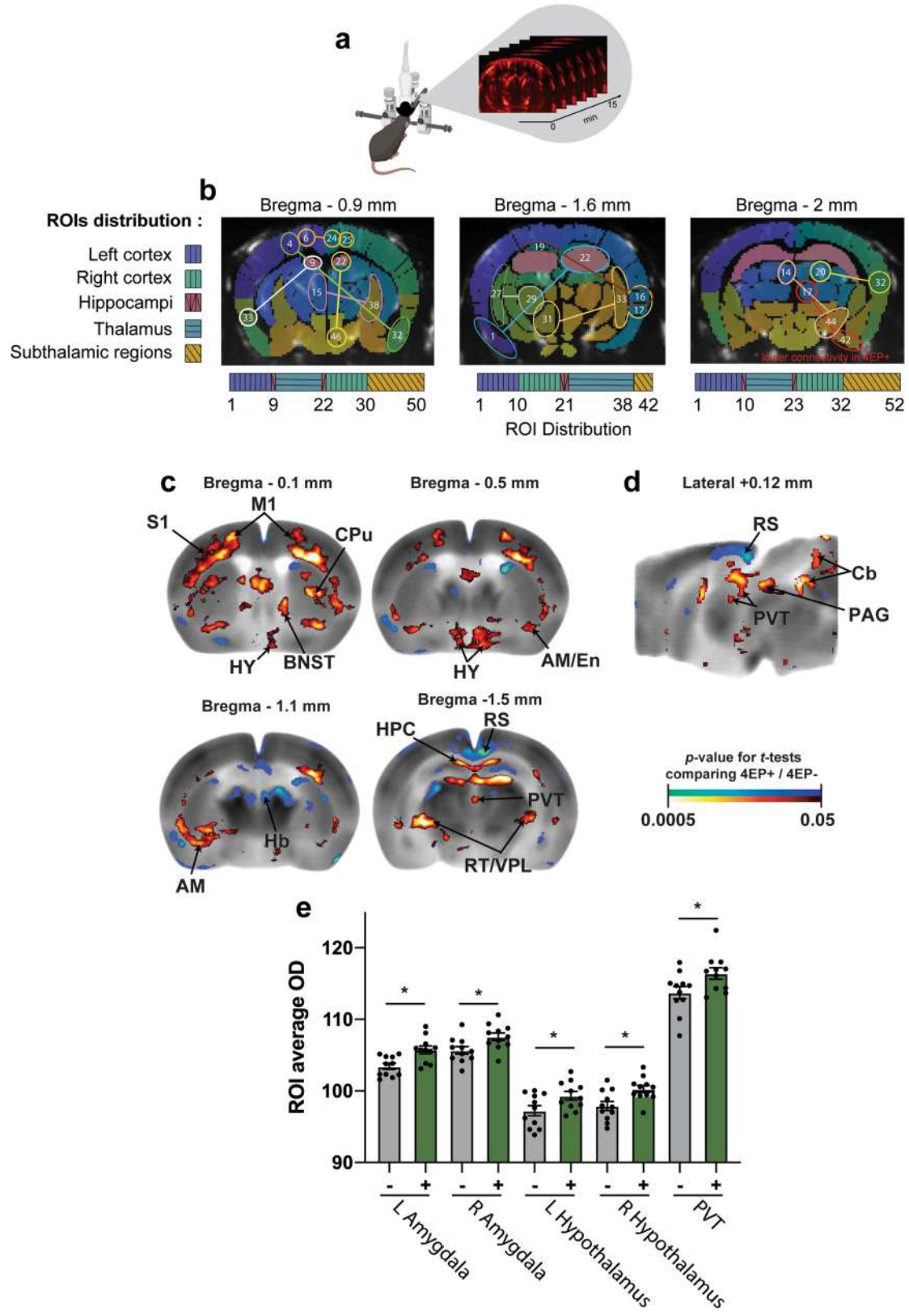


Extended Data Fig. 3 | See next page for caption.

Article

Extended Data Fig. 3 | Lack of inflammatory signals in peripheral and brain cytokine and immune profiles of 4EP^{+/−} mice. **a, b**, Cytokine and chemokine levels presented in bar graph where grey (−) is 4EP[−] and green (+) is 4EP⁺, measured by bioplex in colon (n=9) **a**, and serum (n=9) **b**. No significant differences were observed. **c–d**, Flow cytometry of spleens of 4EP⁺ and 4EP[−] mice. For gating strategy see Supplementary Fig. 2. **c**, Percentages of CD4⁺ or CD8⁺ T cells (4EP[−] n=11, 4EP⁺ n=10). **d**, Percentage of B cells (4EP[−] n=11, 4EP⁺ n=10) $p < 0.0001$. **e**, Cytokine and chemokine levels presented in bar graph where grey (−) is 4EP[−] and green (+) is 4EP⁺, measured by bioplex (n=9) in brain tissue (IL-3 $p = 0.046$; IL-5 $p = 0.01$; KC $p = 0.02$; TNF- α $p = 0.01$). **f**, Flow cytometry

percentages of microglia in the brain of 4EP[−] and 4EP⁺ mice. For gating strategy see Supplementary Fig. 2. **g**, Relative expression of microglial genes in microglial-enriched samples (n=8). Multiple randomized litters were used for the experiments in the figure. Each data point represents biologically independent mice from multiple randomized litters examined over one (a-b) or two (c-h) respective experiments. Data represent mean ± SEM. Panels a, b, d, f, and h were analysed by one-way ANOVA with Dunnett multiple comparisons test comparing each 4EP^{+/−} pair, and panels g and e by a two-tailed Welch's t-test. * $p \leq 0.05$; ** $p \leq 0.01$; *** $p \leq 0.001$.

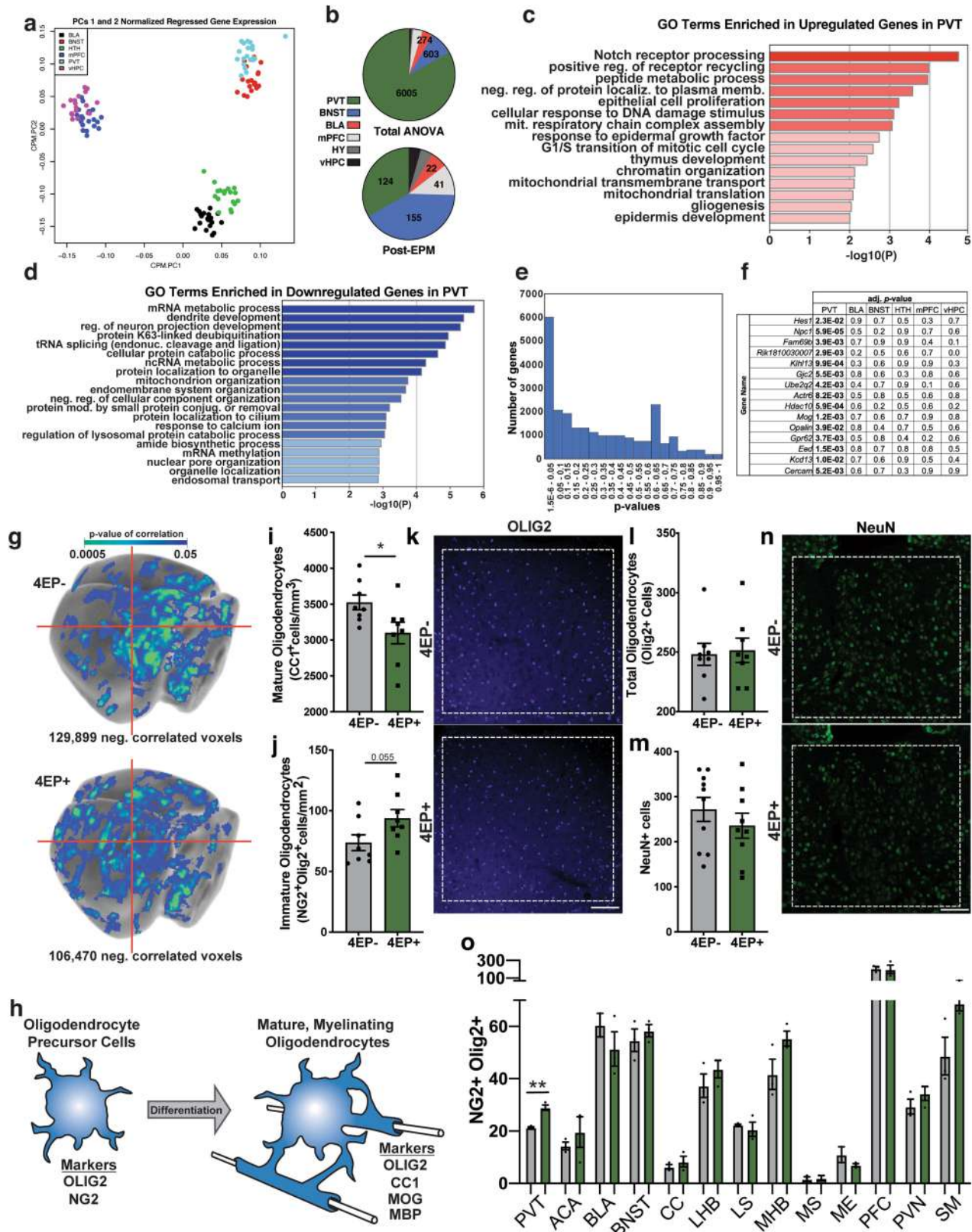


Extended Data Fig. 4 | See next page for caption.

Article

Extended Data Fig. 4 | Extended information on functional connectivity experiments fUSi and autoradiography. **a**, Schematic representation of the functional ultrasound (fUSi) set-up. Functional acquisitions are acquired non-invasively through intact skull and scalp in anaesthetized mice during 15 min per coronal plane. Created with BioRender.com. **b**, Maps overlaid with regions of interest coloured in a gradient for easier visualization. Significant pairs are indicated, corresponding to the data in main Fig. 2b. Three coronal planes per mouse were studied: Bregma -0.9 mm, Bregma -1.6 mm, Bregma -2mm. 50, 52 and 52 ROIs are respectively delineated for each plane according the Paxinos Atlas. Coronal plane B-0.9mm: ROIs #1 to #8 are located in the left cortex, ROI#9 is the left hippocampus, ROIs#11 to #21 are located in the thalamus, ROI#22 is the right hippocampus, ROIs#23 to #30 are located in the right cortex and finally ROIs#31 to #48 are subthalamic regions. Coronal plane B-1.6mm: ROIs #1 to #20 are located in the cortex, ROIs#21#22 are the left and right hippocampi, ROIs#23 to #38 are located in the thalamus and ROIs#39 to #42 are subthalamic regions. Coronal plane B-2mm: ROIs #1 to #9 are located in the left cortex, ROI#10 is the left hippocampus, ROIs#11 to #22 are located in the thalamus, ROI#23 is the right hippocampus, ROIs#24 to #32 are located in the right cortex and finally ROIs#33 to #50 are subthalamic regions.

c–d, Colour-coded overlays over representative coronal (c) and sagittal (d) sections of the mouse brain template showing significant differences in regional cerebral glucose uptake following open field exposure in 4EP⁺ mice compared to 4EP⁻ mice (n=11) (t-test, $p \leq 0.05$, extent threshold > 200 contiguous voxels, with both conditions met to be deemed significant; red/blue: increase/decrease in glucose uptake in 4EP⁺ compared to 4EP⁻ mice). **e**, Quantitated 2DG-uptake by region of interest, including the amygdala, hypothalamus and PVT, confirming changes in relative 2DG uptake in the open field groups (n=11 each group) From left to right, $p = 0.01$; 0.03; 0.02; 0.009; 0.003). Average optical density of each ROI in each animal was normalized to whole-brain average of that animal. Abbreviations: AM, amygdala; HY, hypothalamus; PVT, paraventricular nucleus of the thalamus; BNST, bed nucleus of the stria terminalis; SI, primary somatosensory cortex; CPu, caudate putamen; Hb, habenular nucleus; RT, reticular nucleus of the thalamus; VPL/VPM, Posterior Lateral/Ventral Posterior Medial Thalamus; R, right; L, left. Two cohorts of mice from multiple litters were used for each experiment in this figure. Panel e was analysed by one-way ANOVA with multiple comparison correction and two-stage linear step-up procedure of Benjamini, Krieger and Yekutieli. * $p \leq 0.05$.

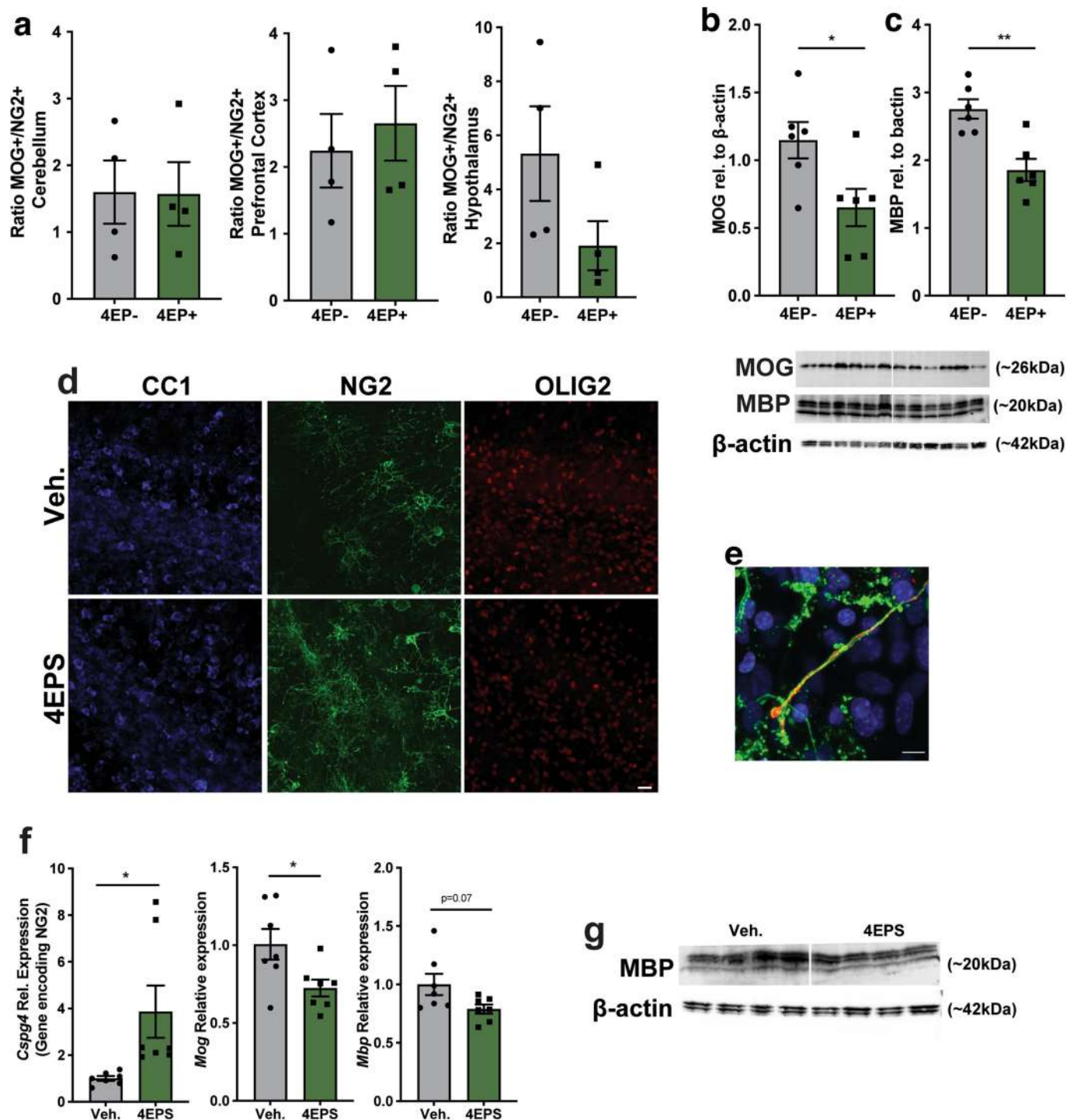


Extended Data Fig. 5 | See next page for caption.

Article

Extended Data Fig. 5 | Extended results of mRNA high throughput sequencing (QuantSeq), and oligodendrocyte analysis by immunofluorescence implicating oligodendrocyte differences in 4EP⁺ mice. **a**, Principal component analysis of all samples analysed by QuantSeq, with tight clustering by brain region. Each brain region is coloured according to the legend. **b**, Differential gene analysis summary showing number of significantly different genes in 6 tested brain regions. Top pie chart refers to total number of differential genes by one-way group ANOVA with all the 4EP⁺ and 4EP⁻, at baseline and post-EPM. The bottom pie chart was generated according to the specific significant ($p<0.05$) contrasts between 4EP⁺ and 4EP⁻ conditions of post-EPM conditions as calculated with the post-hoc Tukey HSD test. **c-d**, GO terms enriched in genes that are upregulated (c) or downregulated (d) in the PVT in 4EP⁺ relative to 4EP⁻ mice in the baseline, home cage condition. X-axis represents -log10(P) of enrichment analysis. **e**, p-value histogram of PVT sequencing at baseline, graphed as p-values binned by 0.05 along the x-axis and number of genes along the y-axis. **f**, Adjusted p-values for 4EP⁺/4EP⁻ comparison of expression of oligodendrocyte specific genes in all 6 brain regions analysed by QuantSeq, corresponding to data presented in Main Fig. 3c for the PVT. $p<0.05$ in bold. **g**, PVT seed analysis correlating 2DG uptake in the PVT to the rest of the brain. Images show 3D rendered, average whole brain correlation data ($n=11$). The centre of the PVT is indicated at the cross section of the red lines, and the number of negatively correlated voxels is shown below in each. Significance is illustrated according to the legend. A minimum threshold of 200 contiguous voxels with $p<0.05$ was used. **h**, Schematic of immature OPC and mature, myelinating oligodendrocyte markers used for immunostaining, flow cytometry, or western blots in this study. **i**, Raw counts of mature oligodendrocytes, measured by CC1⁺ and OLIG2⁺

staining in 4EP⁺ and 4EP⁻ mice in the PVT, used to calculate maturity quotient in Fig. 3f ($n=8$), $p=0.04$. **j**, Raw counts of immature oligodendrocytes, measured by NG2⁺ and OLIG2⁺ staining in 4EP⁺ and 4EP⁻ mice in the PVT, used to calculate maturity quotient in Fig. 3f ($n=8$ each group), $p=0.055$. **k**, Representative images (corresponding to main Fig. 3e, f) of the PVT in brain sections from 4EP⁺ and 4EP⁻ mice, stained for OLIG2, using total cumulative counts from 3-5 images per replicate ($n=8$). Scale bar 100 μ m. **l**, Raw counts of OLIG2⁺ cells in the PVT of 4EP^{+/−} mice. Each data point represents an individual mouse, with total cumulative counts from the PVT ($n=8$) $p=0.8$. **m**, Raw counts of NeuN⁺ staining in the PVT (4EP[−] $n=10$, 4EP⁺ $n=9$), using average counts from 3-5 images per replicate. **n**, Representative images of pan-neuronal NeuN staining in the PVT, with 3-5 images per replicate (4EP[−] $n=10$, 4EP⁺ $n=9$). Scale bar 100 μ m. **o**, NG2⁺ staining in extended regions of the brain ($n=3$ each group) $p=0.009$. Abbreviations: PVT, the paraventricular nucleus of the thalamus; BNST, bed nucleus of the stria terminalis; BLA, basolateral amygdala; mPFC, medial prefrontal cortex; HY, hypothalamus; vHPC, ventral hippocampus; OLIG2, oligodendrocyte transcription factor 2; NG2, neural/glial antigen 2; CC1, antibody (anti-adenomatous polyposis coli (APC) clone) that binds mature oligodendrocyte marker; MOG, myelin oligodendrocyte glycoprotein; MBP, myelin basic protein; ACA, anterior commissure; CC, corpus callosum; LHB, lateral habenula; LS, lateral septum; MHB, medial habenula; MS, medial septum; ME, median eminence; PFC, prefrontal cortex; PVN, paraventricular nucleus of the hypothalamus; SM, stria medullaris of thalamus. Two cohorts of mice from multiple litters were used for experiments in panels g-o in this figure. Data represent mean \pm SEM. Analysis performed using two-tailed Welch's t-tests (i-m) or one-way ANOVA with Dunnett multiple comparison between 4EP^{+/−} pairs (o). * $p\leq 0.05$.



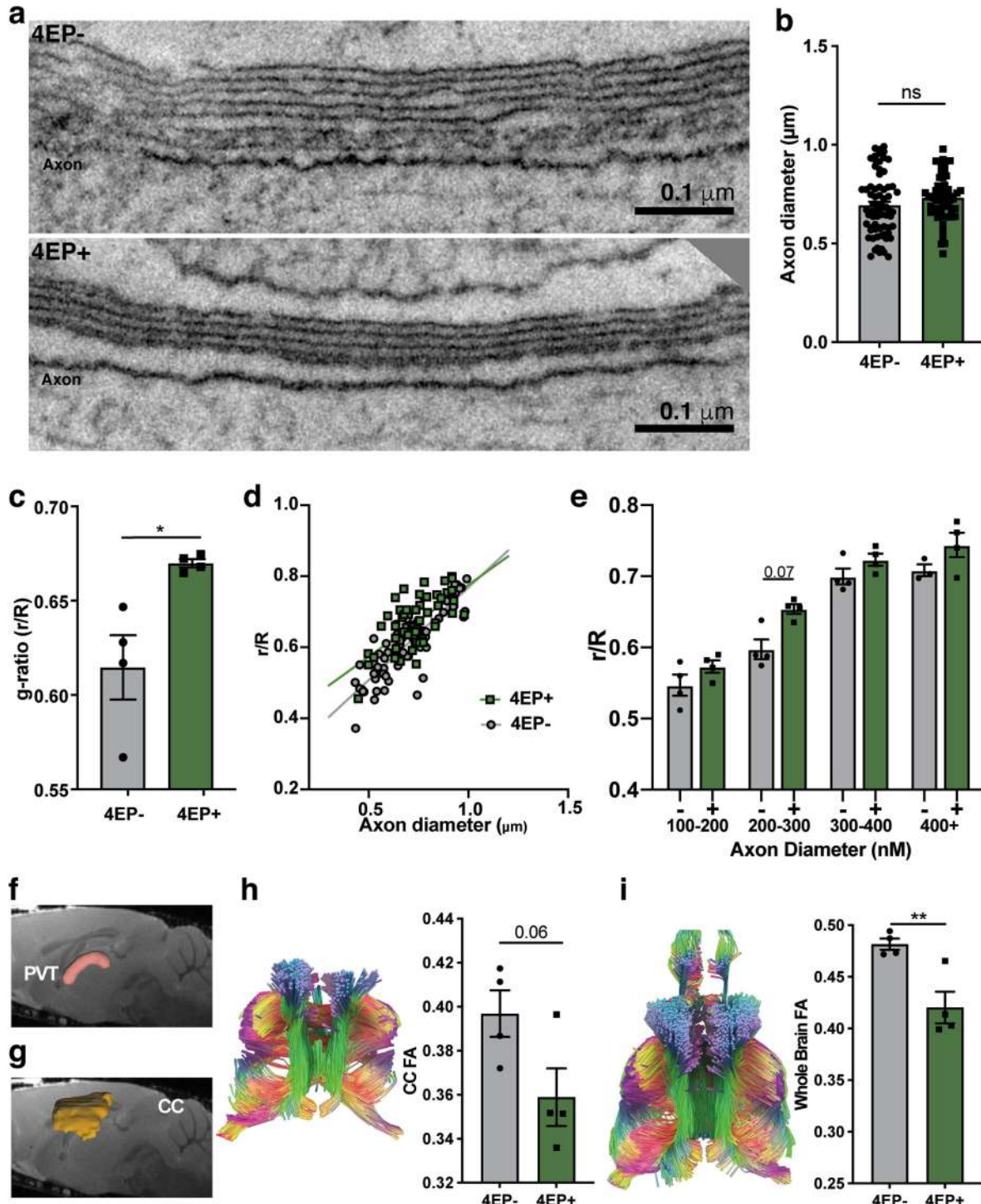
Extended Data Fig. 6 | Extended results of oligodendrocyte analysis implicating oligodendrocyte differences in 4EP⁺ mice *in vivo* and *in vitro*.
a, Extended quantitation of flow cytometry with MOG⁺/NG2⁺ ratio by quadrant in the cerebellum, cortex, and hypothalamus (n=4). **b–c**, Western blot analysis of MOG ($p=0.03$) and MBP ($p=0.002$) markers (respectively) of mature oligodendrocytes from the PVT brain region. PVT punches from two mice were pooled per data point in quantitative data (n=6 pooled samples each group). For gel source data, see Supplementary Fig. 1. **d–g**, Organotypic brain slices were cultured in the presence of 10 μ M 4EPS. **d**, Representative images of CC1, NG2 and Olig2 staining. Two cohorts of mice were used, with each data point in Fig 3i representing quantified images from samples from individual mice. Scale bar 20 μ m. **e**, Example high-magnification image of axon in organotypic brain

slices, stained with antibodies specific to NF (red), and PLP (green), with DAPI (blue), taken from image set used for quantification in 3i and Extended Data Fig. 6d. Scale bar 8 μ m. **f**, qPCR results of oligodendrocyte genes, *Cspg4* ($p=0.04$), *Mog* ($p=0.03$), and *Mpb* from organotypic brain slices (n=7).

g, Western blot image of mature oligodendrocyte marker MBP (quantified in main Fig. 3i). For gel source data, see Supplementary Fig. 1. Abbreviations: NG2, neural/glial antigen 2; CC1, antibody (anti-adenomatous polyposis coli (APC) clone) that binds mature oligodendrocyte marker; MOG, myelin oligodendrocyte glycoprotein; MBP, myelin basic protein. Two cohorts of mice from multiple litters were used for experiments in this figure. Data represent mean \pm SEM. Statistics were performed using two-tailed Welch's t-tests.

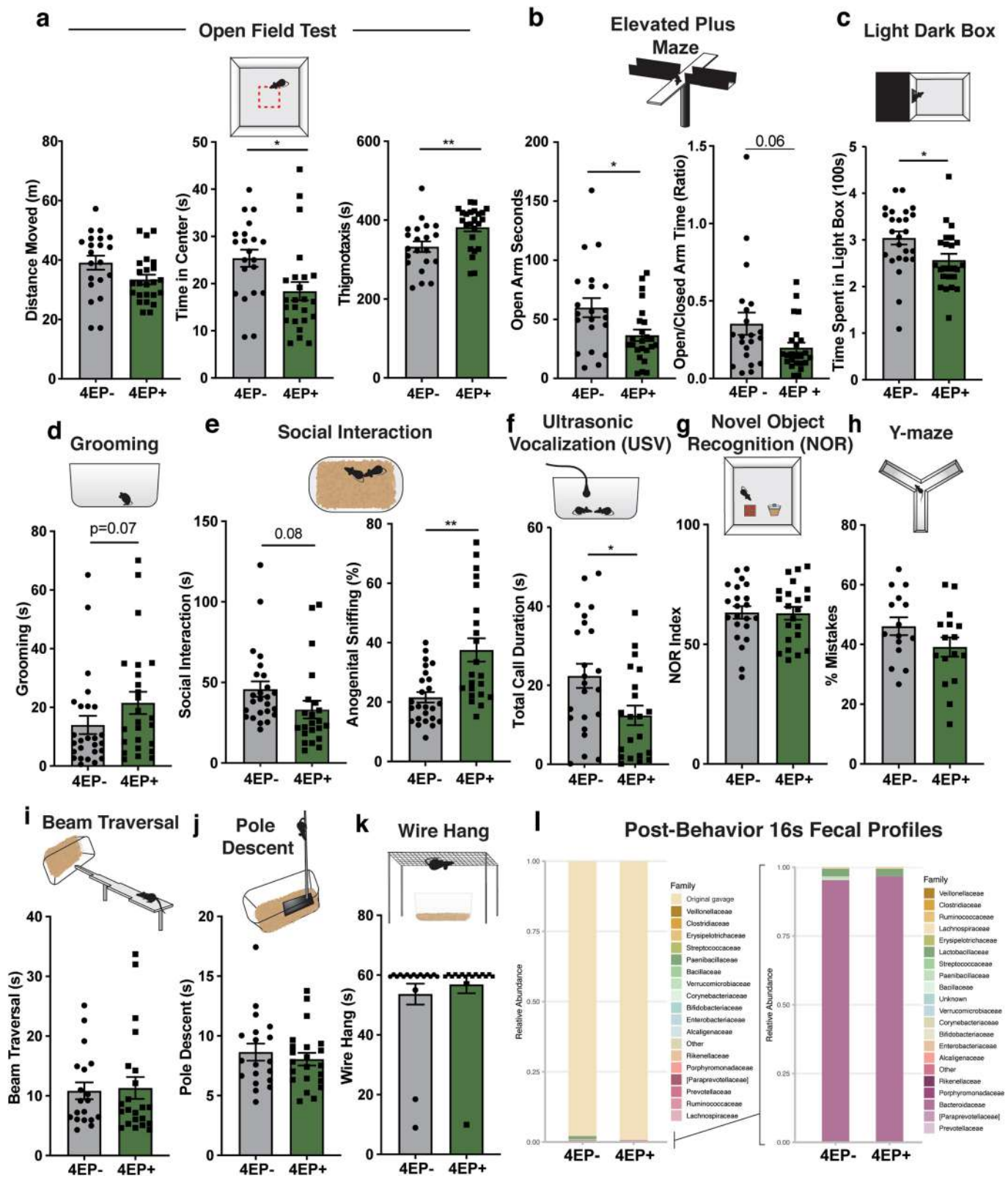
* $p \leq 0.05$; ** $p \leq 0.01$.

Article



Extended Data Fig. 7 | Extended results of myelin analysis by electron microscopy and DTI. **a**, Additional ET of myelinated axons in 4EP⁻ (top) and 4EP⁺ (bottom) mice visualized longitudinally along an axon (n=3; 4 images each). These longitudinal images were used only for qualitative visual assessment of myelin to accompany the other quantitative measures. **b**, Axon diameters (measured from cell membrane, not including myelin layer) from all axons used to calculate g-ratio (4EP⁻, 56; 4EP⁺, 70 axons) (n=4; 4 images each). $p=0.1$. **c**, g-ratio (r/R), the inner axon diameter/outer diameter of the myelin sheath, of 4EP⁺ and 4EP⁻ mice. Each data point represents a mouse (n=4), which is an average of the g-ratio of all axons quantified from 4 images per mouse, where a larger g-ratio indicates a thinner layer of myelin. $p=0.046$. **d**, Plot of g-ratio (r/R) on the y-axis and axon diameter on the x-axis, with linear regression

noted by lines (4EP⁻, 56; 4EP⁺, 70 axons) (n=4; 4 images each). **e**, Average g-ratio of each animal, binned by axon size, indicating that mid-sized range of axons are driving the change in overall g-ratio phenotype observed in the mice (n=4). **f-g**, Defined regions of interest for the PVT and corpus callosum (CC) overlaid on representative sagittal MRI image. **h-i**, representative tracts observed from a bilateral coronal plane view (left) and fractional anisotropy (FA) analysis (right) for the corpus callosum (CC), and whole brain ($p=0.009$, respectively (n=4). Two independent trials using multiple litters were used for experiments in this figure. Data represent mean \pm SEM. Statistics were performed using two-tailed Welch's t-tests (b,c,h,i), simple linear regression test (d), or one-way ANOVA with Dunnett multiple comparison between 4EP^{+/−} groups at each size group. * $p \leq 0.05$; ** $p \leq 0.01$.



Extended Data Fig. 8 | See next page for caption.

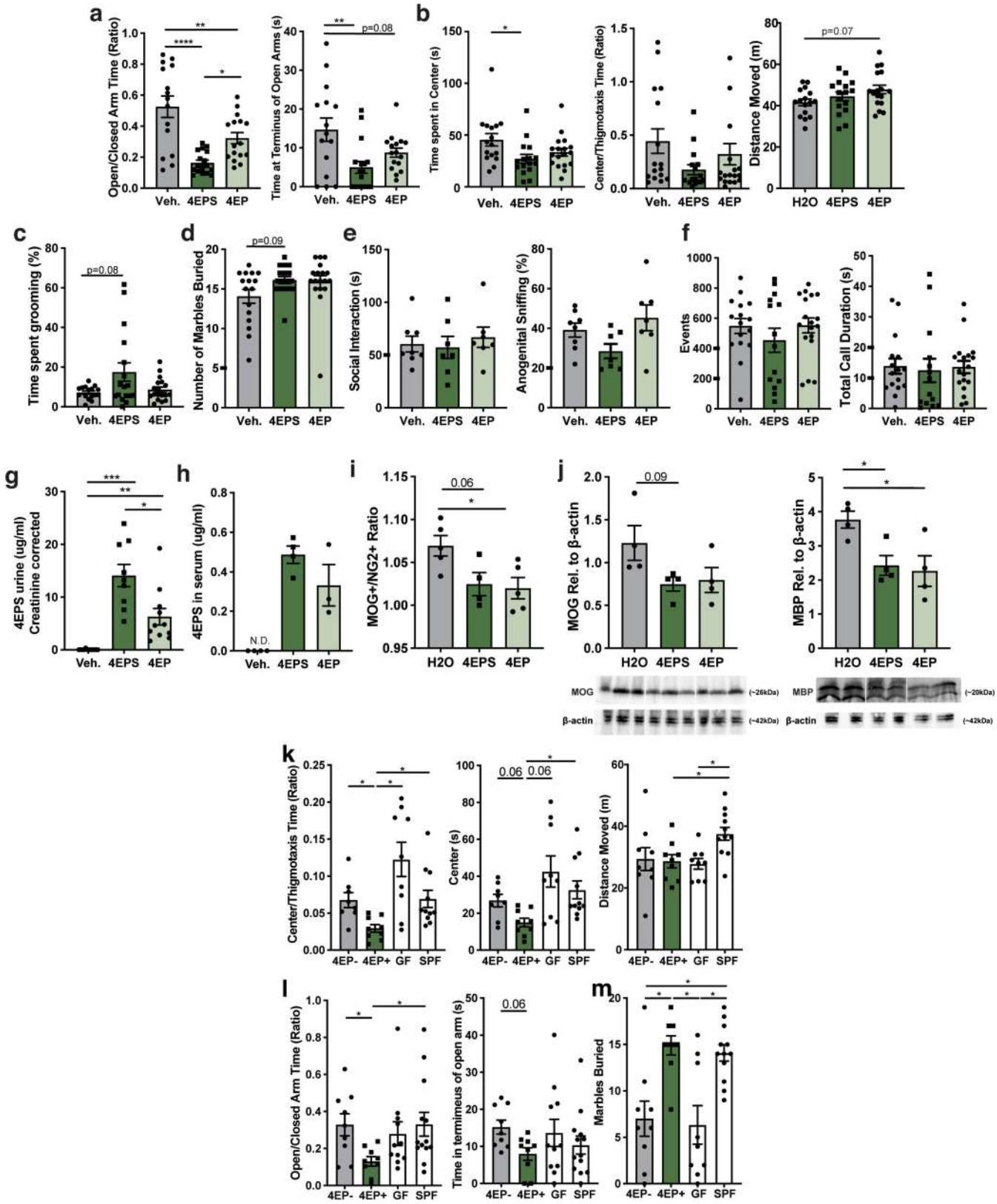
Article

Extended Data Fig. 8 | Additional behaviour tests in 4EP⁻ and 4EP⁺ mice.

a, Distance traveled ($p=0.06$), time in centre ($p=0.01$), and thigmotaxis time ($p=0.007$), during open field test over a period of 10 min (distance traveled data was also shown in Extended Data Fig. 2g) (4EP⁻ n=21, 4EP⁺ n=24). **b**, Time spent in the open arms of the elevated plus maze (EPM) (left) ($p=0.02$) and ratio of time spent in the open/time spent in the closed arms of the EPM (right) (4EP⁻ n=21, 4EP⁺ n=24). **c**, Light/dark box: time mice spent in the open, lit portion of the arena. Test time, 10 min (4EP⁻ n=25, 4EP⁺ n=23) $p=0.02$. **d**, Grooming: total time mice spent self-grooming over a period of 10 min (4EP⁻ n=27, 4EP⁺ n=24). **e**, Social interaction: with an unfamiliar, age-matched male intruder. Total time socializing (left) and percent of total socializing that is anogenital sniffing (right) (4EP⁻ n=25, 4EP⁺ n=22) $p=0.0009$. **f**, Ultrasonic vocalization: time spent vocalizing to an unfamiliar, age-matched female for 3 min (4EP⁻ n=23, 4EP⁺ n=21) $p=0.01$. **g**, Novel object recognition (NOR): time spent investigating a

novel object when presented with a novel and a familiar object (n=22).

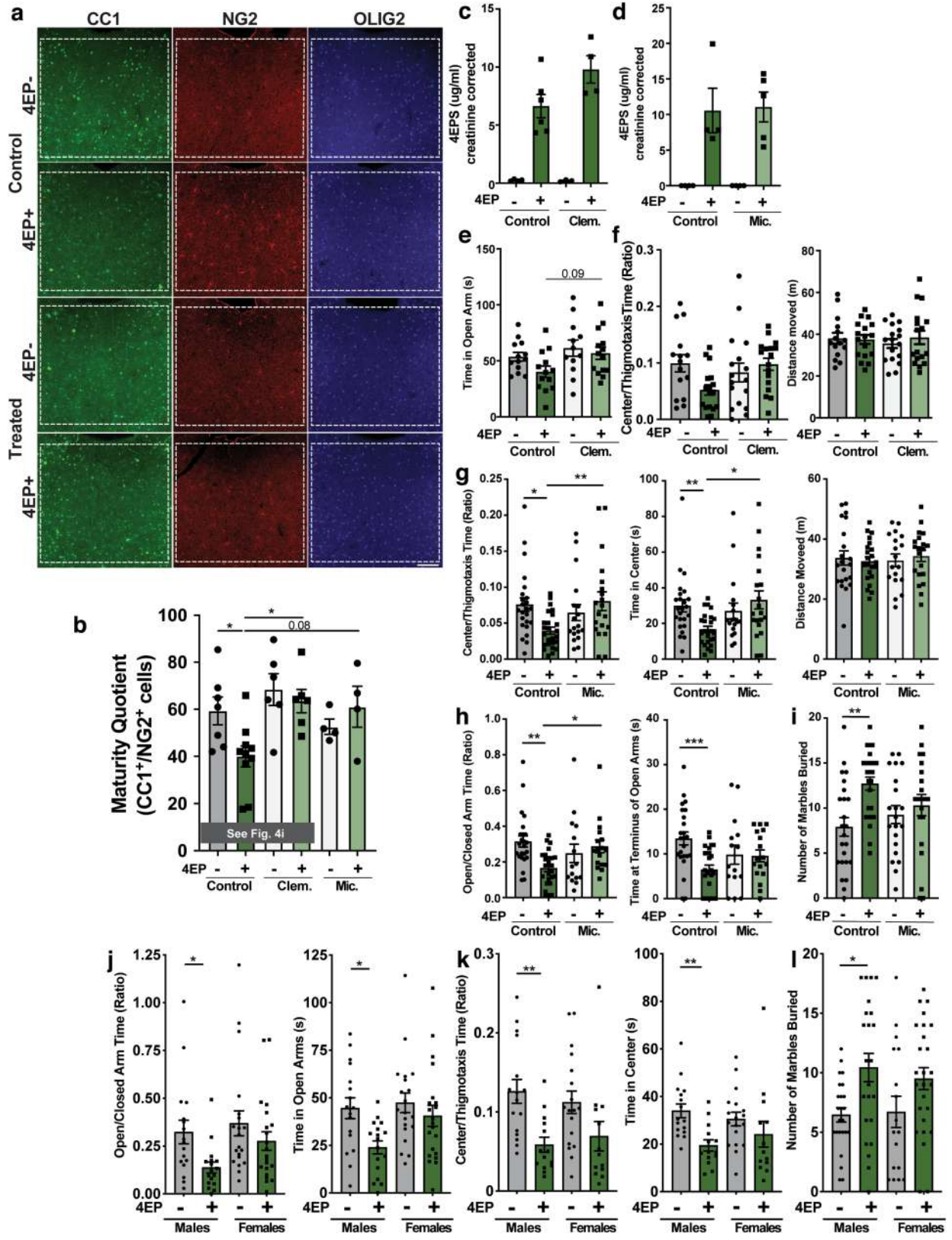
h, Y-maze alternations: percent of times mice repeated entry into an arm it had just visited rather than alternate to all arms in succession (4EP⁻ n=15, 4EP⁺ n=16). **i**, Beam traversal: time required for the mouse to cross the narrowing beam (4EP⁻ n=19, 4EP⁺ n=22). **j**, Pole descent: time required for the mouse to descend from the pole to the home cage (4EP⁻ n=19, 4EP⁺ n=22). **k**, Wire hang: time the mouse hung on and explored the underside of the wire grid before releasing into cage below (4EP⁻ n=19, 4EP⁺ n=22). **l**, Faecal 16S profiles of 4EP^{+/−} mice after behaviour tests, where tan is the colonization group and contamination from exposure to behaviour tests is coloured according to the legend (left panel) and a magnified view of contaminants only (right panel) (4EP⁻ n=8, 4EP⁺ n=10). Two independent cohorts of mice from multiple litters were used for each experiment in this figure. Data a-k represent mean ± SEM analysed by two-tailed Welch's t-test. * $p \leq 0.05$; ** $p \leq 0.01$.



Extended Data Fig. 9 | See next page for caption.

Article

Extended Data Fig. 9 | Behaviour results from 4EP or 4EPS administration by drinking water and anxiety behaviour tests of 4EP+/- mice relative to GF and SPF mice. **a–f**, Behaviour tests of conventionally colonized mice administered 4EP or 4EPS by drinking water. **a**, Left panel: EPM, time spent in open arms over time spent in closed arms (seconds). Right panel: time spent at terminus (outer 1/3 of open arms) (Veh. n=15; 4EPS n=17; 4EP n=16) (Open/closed: Veh. vs 4EPS $p<0.0001$; Veh vs 4EP $p=0.007$; 4EPS vs 4EP $p=0.03$; Terminus: Veh vs 4EPS $p=0.004$). **b**, Open field test, from left to right: time spent in the centre area over thigmotaxis, time spent in centre (seconds), distance moved in open field test, showing an increase in activity in 4EP-treated animals (Veh. n=16; 4EPS n=16; 4EP n=18) $p=0.02$. **c**, Grooming test, total percent of time spent grooming, showing an increase in grooming in the 4EPS-treated animals (Veh. n=16; 4EPS n=18; 4EP n=17). **d**, Number of marbles buried (Veh. n=16; 4EPS n=17; 4EP n=18). **e**, Social interaction. Left panel: total socialization time (seconds). Right panel: % of total socialization time spent as anogenital sniffing (Veh. n=8; 4EPS n=7; 4EP n=7). **f**, USV test. Left panel: Vocalization events. Right panel: Total duration spent vocalizing (seconds) (Veh. n=16; 4EPS n=15; 4EP n=18). **g**, 4EPS levels in urine of mice administered 4EP or 4EPS in the drinking water (creatinine corrected) (Veh. n=12; 4EPS n=9; 4EP n=11) (Veh. vs 4EPS $p=0.0005$; Veh vs 4EP $p=0.008$; 4EPS vs 4EP $p=0.03$). **h**, 4EPS levels in serum of mice administered 4EP or 4EPS in the drinking water (Veh. n=4; 4EPS n=4; 4EP n=3). **i**, Quantified flow cytometry data of PVT of mice administered 4EP or 4EPS in the drinking water, with ratio of MOG+ quartile percentages/NG2+ quartile percentages presented (Veh. n=5; 4EPS n=5; 4EP n=4) $p=0.03$. For gating strategy see Supplementary Fig. 2 and main Fig. 3h. **j**, Quantified western blot data for MOG and MBP in the PVT of mice administered 4EP or 4EPS in the drinking water, with blots shown below (n=4 each group). (MBP: H2O vs 4EPS $p=0.04$; vs 4EP $p=0.02$). For gel source data, see Supplementary Figure 1. **k–m**, Anxiety behaviour tests contextualizing 4EP+/- mice to GF and SPF mice. **k**, Open field test, from left to right: time spent in the centre area over time spent along walls (4EP- vs 4EP+ $p=0.04$; 4EP+ vs GF $p=0.02$; 4EP+ vs SPF $p=0.04$), time spent in the centre (seconds), distance moved in open field test (4EP- vs SPF $p=0.047$; GF vs SPF $p=0.01$) (4EP- n=8; 4EP+ n=9; GF n=9; SPF n=11). **l**, Elevated plus maze, time spent in the open arms/time spent in the closed arms ration (left) (4EP- vs 4EP+ $p=0.03$; 4EP+ vs SPF $p=0.03$) and time spent at the terminus (right) (4EP- n=9; 4EP+ n=9; GF n=11; SPF n=13). **m**, Marble burying (4EP- n=9; 4EP+ n=9; GF n=9; SPF n=11) (4EP- vs 4EP+ $p=0.02$; 4EP- vs SPF $p=0.03$; 4EP+ vs GF $p=0.02$; GF vs SPF $p=0.03$). Abbreviations: Veh., vehicle control; MOG, myelin oligodendrocyte glycoprotein; MBP, myelin basic protein. Two independent cohorts of mice from multiple litters were used for the experiments in this figure. Data represent mean \pm SEM analysed by one-way ANOVA with Dunnett multiple comparison between all groups. * $p\leq0.05$; ** $p\leq0.01$; *** $p\leq0.001$; **** $p\leq0.0001$.



Extended Data Fig. 10 | See next page for caption.

Article

Extended Data Fig. 10 | Fluorescence imaging and extended behaviour test results of clemastine fumarate and miconazole-treated mice, and preliminary behaviour tests performed on both sexes, used to determine continued studies on males for the study. **a–i**, 4EP^{+/−} mice were administered vehicle (control), clemastine fumarate (clem.), or miconazole and then behaviour tested and imaged. **a**, Representative images of CC1 (green), NG2 (red), and OLIG2 (blue) staining in 4EP^{+/−} mice with or without treatment. Representative of group of individual mice used for quantification: 4EP[−] control=7, treated=10; 4EP⁺ control=6, treated=6, which came from two cohorts (Scale bar 100 µm). **b**, Quantification of fluorescent imaging, presented as a ratio of CC1⁺/NG2⁺ cells (from left to right n=7, 10, 6, 6, 4, 4). The first four columns are also shown in Main Fig. 4i (Cont 4EP[−] vs 4EP⁺ p=0.04; 4EP[−] Cont vs 4EP⁺ Clem p=0.01). **c–d**, Confirmation that treatment does not reduce 4EPS levels with clemastine (c) (Control, 4EP[−] n=4; Control, 4EP⁺ n=6; Clem 4EP[−] n=3; Clem 4EP⁺ n=4) or miconazole (d) (Control, 4EP[−] n=4; Control, 4EP⁺ n=4; Mic 4EP[−] n=4; Mic 4EP⁺ n=5) treatment. **e**, Extended EPM results (Control 4EP[−] n=13; Control 4EP⁺ n=13; Clem 4EP[−] n=12; Clem 4EP⁺ n=14). **f**, Extended open field results (Control 4EP[−] n=15; Control 4EP⁺ n=17; Clem 4EP[−] n=17; Clem 4EP⁺ n=17). **g–i**, Behavioural results for mice treated with miconazole, including **g**, Open field (Control 4EP[−] n=24; Control 4EP⁺ n=25; Mic, 4EP[−] n=18; Mic, 4EP⁺ n=20)(left graph: 4EP[−] Cont vs 4EP⁺ Cont p=0.02; 4EP[−] cont vs 4EP⁺ Mic p=0.008)(middle graph: 4EP[−] Cont vs 4EP⁺ Cont p=0.02; 4EP[−] cont vs 4EP⁺ Mic p=0.005). **h**, EPM (Control 4EP[−] n=24; Control 4EP⁺ n=25; Mic, 4EP[−] n=15; Mic, 4EP⁺ n=17)(left graph: 4EP[−] Cont vs 4EP⁺ Cont p=0.002; 4EP[−] cont vs 4EP⁺ Mic p=0.03)(right graph: 4EP[−] Cont vs 4EP⁺ Cont p=0.0009). **i**, Marble Burying (Control 4EP[−] n=24; Control 4EP⁺ n=26; Mic, 4EP[−] n=21; Mic, 4EP⁺ n=21) (p=0.001) **j**, Left panel: EPM, time spent in open arms over time spent in closed arms. Right panel: time spent at terminus (outer 1/3 of open arms) (Males 4EP[−] n=17; Males 4EP⁺ n=17; Females 4EP[−] n=20; Females 4EP⁺ n=21) p=0.02. **k**, Open field test, time spent in the centre area over time spent in thigmotaxis (left), time spent in the centre (right) (Males 4EP[−] n=16; Males 4EP⁺ n=14; Females 4EP[−] n=18; Females 4EP⁺ n=13) p-values left to right: 0.005, 0.003. **l**, Number of marbles buried in marble burying test (Males 4EP[−] n=24; Males 4EP⁺ n=23; Females 4EP[−] n=17; Females 4EP⁺ n=26) p=0.03. Abbreviations: NG2, neural/glial antigen 2; CC1, antibody (anti-adenomatous polyposis coli (APC) clone) that binds mature oligodendrocyte marker; OLIG2, oligodendrocyte transcription factor 2; clem, clemastine fumarate; mic, miconazole. Two independent cohorts of mice from multiple litters were used for each experiment in this figure. Data represent mean ± SEM analysed by two-way ANOVA with Dunnett multiple comparison to 4EP⁺ group (panels b–i) or Sidak multiple comparison between 4EP^{+/−} groups within each sex (panels j–l). *p≤0.05, **p≤0.01.

Reporting Summary

Nature Research wishes to improve the reproducibility of the work that we publish. This form provides structure for consistency and transparency in reporting. For further information on Nature Research policies, see our [Editorial Policies](#) and the [Editorial Policy Checklist](#).

Statistics

For all statistical analyses, confirm that the following items are present in the figure legend, table legend, main text, or Methods section.

n/a Confirmed

- The exact sample size (n) for each experimental group/condition, given as a discrete number and unit of measurement
- A statement on whether measurements were taken from distinct samples or whether the same sample was measured repeatedly
- The statistical test(s) used AND whether they are one- or two-sided
Only common tests should be described solely by name; describe more complex techniques in the Methods section.
- A description of all covariates tested
- A description of any assumptions or corrections, such as tests of normality and adjustment for multiple comparisons
- A full description of the statistical parameters including central tendency (e.g. means) or other basic estimates (e.g. regression coefficient) AND variation (e.g. standard deviation) or associated estimates of uncertainty (e.g. confidence intervals)
- For null hypothesis testing, the test statistic (e.g. F , t , r) with confidence intervals, effect sizes, degrees of freedom and P value noted
Give P values as exact values whenever suitable.
- For Bayesian analysis, information on the choice of priors and Markov chain Monte Carlo settings
- For hierarchical and complex designs, identification of the appropriate level for tests and full reporting of outcomes
- Estimates of effect sizes (e.g. Cohen's d , Pearson's r), indicating how they were calculated

Our web collection on [statistics for biologists](#) contains articles on many of the points above.

Software and code

Policy information about [availability of computer code](#)

Data collection Ethovision XT4 and 10 (Noldus Information Technology; Leesburg, VA, USA); SPM, version 5, Wellcome Centre for Neuroimaging, University College London, London, UK); Zen software 2.3.69.1018 (Carl Zeiss, Oberkochen, Germany); BBDuk (Version 37.90; <http://jgi.doe.gov/data-and-tools/bb-tools/>); STAR (Version 2.5.2b); Salmon (Version 0.7.2); Picard (Version 2.5.0); MOD software package for MacPro and iMacPro computers; Agilent 1260 LC system coupled to an Agilent 6120 quadrupole mass spectrometer with a 3 µm, 4.6 x 75 mm Unison UK-C18 column (Imtakt, Portland, OR); Agilent 7890 GC coupled to an Agilent 5977 MSD with a HP-5MS fused silica capillary column (30m x 250 µm x 0.25 µm) (Portland, OR); Bio-Plex 200 Systems instrument; 15 MHz ultrasonic ultralight probe prototype (15 MHz, 64 elements, 0.110 mm pitch, Vermon, Tours, France) connected to a Verasonics Vantage ultrasound system (Verasonics Inc., Redmond, WA, USA); Illumina HiSeq 2500; CytoFLEX S Flow Cytometer ; Bruker Avance Neo 7T/30 scanner, Bruker gradient and shim unit (B-GA12SHP insert for BGA20); TF-30ST transmission electron microscope (Thermo Fisher Scientific, Waltham, MA)

Data analysis NCBI Blast (<https://blast.ncbi.nlm.nih.gov/Blast.cgi>); Excel For Mac v16.37; Graphpad prism 8; Ethovision XT4 and 10 (Noldus Information Technology; Leesburg, VA, USA); SPM, version 5, Wellcome Centre for Neuroimaging, University College London, London, UK); Zen software version 2.3.69.1018 (Carl Zeiss, Oberkochen, Germany); BBDuk (Version 37.90; <http://jgi.doe.gov/data-and-tools/bb-tools/>); STAR (Version 2.5.2b); Salmon (Version 0.7.2); Picard (Version 2.5.0); R (pSI package); Go-Elite; Metascape (metascape.org); MOD software package for MacPro and iMacPro computers; FlowJo v10.6.2; WOL database: <https://biocore.github.io/wol/download>; Greengenes database: <https://greengenes.secondgenome.com/>; Qiime 2; Matlab (MathWorks, USA); TurboReg, an automated pixel-based registration algorithm implemented in ImageJ (version 1.35, <http://rsbweb.nih.gov/ij/>); MRIcro (version 1.40, <https://people.cas.sc.edu/orden/micro/micro.html>); Illumina bcl2fastq (version 2.18.0.12); Bruker PV360 ; DSI Studio software package (<http://dsi-studio.labsolver.org/>)

For manuscripts utilizing custom algorithms or software that are central to the research but not yet described in published literature, software must be made available to editors and reviewers. We strongly encourage code deposition in a community repository (e.g. GitHub). See the Nature Research [guidelines for submitting code & software](#) for further information.

Data

Policy information about [availability of data](#)

All manuscripts must include a [data availability statement](#). This statement should provide the following information, where applicable:

- Accession codes, unique identifiers, or web links for publicly available datasets
- A list of figures that have associated raw data
- A description of any restrictions on data availability

All data analyzed for this study is included in this published article with source data for all figures in the supplementary information files, with additional further 2DG data available upon request. The WoL database annotation files are publicly available at: <https://biocore.github.io/wol/download>. Greengenes database is publicly available at: <https://greengenes.secondgenome.com/>.

Field-specific reporting

Please select the one below that is the best fit for your research. If you are not sure, read the appropriate sections before making your selection.

Life sciences Behavioural & social sciences Ecological, evolutionary & environmental sciences

For a reference copy of the document with all sections, see nature.com/documents/nr-reporting-summary-flat.pdf

Life sciences study design

All studies must disclose on these points even when the disclosure is negative.

Sample size	We used the largest sample sizes possible given the prohibitive space for germ-free and animal colonies, as well as limiting use of animals as much as possible. Due to this limitation in number, no sample size calculation was performed. For animal behavior experiments, two experiments are provided. Behavior experiments typically require large sample sizes ($n>8$) due to inherent biological variability.
Data exclusions	No data was intentionally excluded from the publication, with the exception of additional results of the Quantseq experiments that were not relevant to the results described in the manuscript, but we are happy to provide upon request.
Replication	All experiments were successfully replicated at least two times with independent biological samples.
Randomization	Animals were randomly assigned to groups by splitting up litters as equally as possible and balancing the groups by birth date.
Blinding	Behavior tests were scored automatically by Ethovision software, or in the case of manual scoring by a trained researcher, the scorer was blinded to group identity. 2DG and fUSi experiments were blinded prior to imaging. Additional experiments, including MRI, and additional experiments dealing with sample analysis, samples were labeled numerically rather than with group identity, but not officially blinded, as analysis was not influenced by human interpretation of data nor handling of animals.

Reporting for specific materials, systems and methods

We require information from authors about some types of materials, experimental systems and methods used in many studies. Here, indicate whether each material, system or method listed is relevant to your study. If you are not sure if a list item applies to your research, read the appropriate section before selecting a response.

Materials & experimental systems

n/a	Involved in the study
<input type="checkbox"/>	<input checked="" type="checkbox"/> Antibodies
<input checked="" type="checkbox"/>	<input type="checkbox"/> Eukaryotic cell lines
<input checked="" type="checkbox"/>	<input type="checkbox"/> Palaeontology and archaeology
<input type="checkbox"/>	<input checked="" type="checkbox"/> Animals and other organisms
<input checked="" type="checkbox"/>	<input type="checkbox"/> Human research participants
<input checked="" type="checkbox"/>	<input type="checkbox"/> Clinical data
<input checked="" type="checkbox"/>	<input type="checkbox"/> Dual use research of concern

Methods

n/a	Involved in the study
<input checked="" type="checkbox"/>	<input type="checkbox"/> ChIP-seq
<input type="checkbox"/>	<input checked="" type="checkbox"/> Flow cytometry
<input type="checkbox"/>	<input checked="" type="checkbox"/> MRI-based neuroimaging

Antibodies

Antibodies used

Western blot antibodies: Antibody titrations were 1:500 for primary antibodies and 1:5,000 for fluorescent conjugated secondary antibodies. Antibodies included: mouse anti-MOG (CL2858, Thermo Fisher Scientific, Waltham, MA), chicken anti-MBP (CH2212, Neuromics, Edina, MN), rabbit anti-β-actin (13E5, Cell Signaling, Danvers, MA), 2° anti-chicken-488 (ab150173, abcam, Cambridge, UK); 2° anti-mouse-488 (ab150113, abcam, Cambridge, UK); 2° anti-rabbit-647 (A31573, Thermo Fisher Scientific, Waltham, MA).

Immunostaining primary antibodies and their dilutions were: mouse anti-NeuN (1:1000; MAB377; Millipore Sigma, Burlington, MA), goat anti-Olig2 (1:500; AF2418; R&D Systems, Minneapolis, MN); mouse anti-CC1 (1:250; NB600-1021; Novus Biologicals, Littleton, CO); rabbit anti-NG2 (1:300; AB5320; Millipore Sigma, Burlington, MA); chicken anti-MBP (1:250; CH22112; Neuromics, Edina, MN); mouse anti-neurofilament (1:250; 837802; Biolegend, San Diego, CA). The fluorescent-conjugated secondary antibodies were donkey anti-goat (1:1000; A-32814, A-21082, A11057; ThermoFisher Scientific, Waltham, MA), donkey anti-rabbit (1:1000; A-21206, A-10042, A-31573; ThermoFisher Scientific, Waltham, MA), and donkey anti-mouse (1:1000; A-21202, A-10037, A-31571; ThermoFisher Scientific, Waltham, MA), and donkey anti-chicken (1:1000; A-11041; A-11039; A-21449, Thermo Fisher Scientific, Waltham, MA).

Flow antibodies used include: anti-NG2 (1:400; Alexa488; Ebioscience, San Diego, CA) and anti-MOG (1:100; biotinylated, Novus Biologicals, Littleton, CO), anti-CX3Cr1 (1:500, PE-Cy7, Biolegend, San Diego, CA), anti-CD45.2 (1:500, PerCP-Cy5.5, Tonbo, San Diego, CA), anti-CD11b (1:500, PE, Biolegend San Diego, CA), anti-CD19 (1:500, FITC, Biolegend, San Diego, CA), anti-CD3e (1:500, PE, ThermoFisher, Waltham, MA), anti-CD4 (1:500, APC, Biolegend, San Diego, CA), anti-TCR β (1:500, PerCP-Cy5.5, Tonbo, San Diego, CA), anti-CD8a (1:500, APC-Cy7, ThermoFisher, Waltham, MA), and streptavidin antibody (1:1000; SAV Alexa 647, 405237, Biolegend, San Diego, CA).

Validation

Manufacturers recommendations were used and titrated as needed to ensure positive staining and low background.

mouse anti-MOG (1:500, CL2858, Thermo Fisher Scientific, Waltham, MA), <https://www.thermofisher.com/antibody/product/MOG-Antibody-clone-CL2858-Monoclonal/MA5-24645>

chicken anti-MBP (1:500, CH22112, Neuromics, Edina, MN), <https://www.neuromics.com/CH22112>

rabbit anti- β -actin (1:500, 13E5, Cell Signaling, Danvers, MA), <https://www.cellsignal.com/products/primary-antibodies/b-actin-13e5-rabbit-mab/4970>

2° anti-chicken-488 (1:5000, ab150173, abcam, Cambridge, UK), <https://www.abcam.com/goat-chicken-igg-hl-alex-fluor-488-preadsorbed-ab150173.html>

2° anti-mouse-488 (1:5000, ab150113, abcam, Cambridge, UK); <https://www.abcam.com/goat-mouse-igg-hl-alex-fluor-488-ab150113.html>

2° anti-rabbit-647 (1:5000, A31573, Thermo Fisher Scientific, Waltham, MA), [https://www.thermofisher.com/order/genome-database/generatePdf?productName=Rabbit%20IgG%20\(H+L\)&assayType=PRANT&productId=A-31573&detailed=true](https://www.thermofisher.com/order/genome-database/generatePdf?productName=Rabbit%20IgG%20(H+L)&assayType=PRANT&productId=A-31573&detailed=true)

mouse anti-NeuN (1:1000; MAB377; Millipore Sigma, Burlington, MA), https://www.emdmillipore.com/US/en/product/Anti-NeuN-Antibody-clone-A60,MM_NF-MAB377

goat anti-Olig2 (1:500; AF2418; R&D Systems, Minneapolis, MN); https://www.rndsystems.com/products/human-mouse-rat-olig2-antibody_af2418

mouse anti-CC1 (1:250; NB600-1021; Novus Biologicals, Littleton, CO); https://www.novusbio.com/products/apc-antibody-cc-1_nb600-1021

rabbit anti-NG2 (1:300; AB5320; Millipore Sigma, Burlington, MA); https://www.emdmillipore.com/US/en/product/Anti-NG2-Chondroitin-Sulfate-Proteoglycan-Antibody_MM_NF-AB5320

chicken anti-MBP (1:500, CH22112, Neuromics, Edina, MN), <https://www.neuromics.com/CH22112>

mouse anti-neurofilament (1:250; 837802; Biolegend, San Diego, CA), <https://www.biolegend.com/en-us/products/anti-neurofilament-marker-pan-neuronal-cocktail-11132?GroupID=BLG15643>

donkey anti-goat (1:1000; A-32814, A-21082, A11057; ThermoFisher Scientific, Waltham, MA), <https://www.thermofisher.com/antibody/secondary/query/filter/host/Donkey/species/Goat>

donkey anti-rabbit (1:1000; A-21206, A-10042, A-31573; ThermoFisher Scientific, Waltham, MA), <https://www.thermofisher.com/antibody/secondary/query/filter/host/Donkey/species/Rabbit>

donkey anti-mouse (1:1000; A-21202, A-10037, A-31571; ThermoFisher Scientific, Waltham, MA), <https://www.thermofisher.com/antibody/secondary/query/filter/host/Donkey/species/Mouse>

donkey anti-chicken (1:1000; A-11041; A-11039; A-21449, Thermo Fisher Scientific, Waltham, MA), <https://www.thermofisher.com/antibody/secondary/query/filter/host/Donkey/species/Chicken>

anti-NG2 (1:400; 9.2.27, Alexa488; Ebioscience, San Diego, CA), <https://www.thermofisher.com/antibody/product/Neural-Glia-Antigen-2-NG2-Antibody-clone-9-2-27-Monoclonal/53-6504-82>

anti-MOG (1:100; 296829, biotinylated, Novus Biologicals, Littleton, CO), https://www.novusbio.com/products/mog-antibody-296829_bam2439

anti-CX3Cr1 (1:500, SA011FA11 PE-Cy7, Biolegend, San Diego, CA), <https://www.biolegend.com/en-us/products/pe-cyanine7-anti-mouse-cx3cr1-antibody-11909?GroupID=BLG13324>

anti-CD45.2 (1:500, H130, PerCP-Cy5.5, Tonbo, San Diego, CA), <https://tonbobio.com/products/percp-cyanine5-5-anti-human-cd45-h130>

anti-CD11b (1:500, ICRF44 PE, Biolegend San Diego, CA), <https://www.biolegend.com/en-us/search-results/pe-anti-human-cd11b antibody-14022?GroupID=BLG15288>

anti-CD19 (1:500, MB19-1, FITC, Biolegend, San Diego, CA), <https://www.biolegend.com/en-us/products/fitc-anti-mouse-cd19 antibody-1971?GroupID=BLG4752>

anti-CD3e (1:500, 17A2 PE, ThermoFisher, Waltham, MA), <https://www.thermofisher.com/antibody/product/CD3-Antibody-clone-17A2-Monoclonal/14-0032-82>

anti-CD4 (1:500, RPA-T4 APC, Biolegend, San Diego, CA), <https://www.biolegend.com/en-us/products/apc-anti-human-cd4 antibody-823?GroupID=BLG7755>

anti-TCR β (1:500, H57-597, PerCP-Cy5.5, Tonbo, San Diego, CA), <https://tonbobio.com/products/percp-cyanine5-5-anti-mouse-tcr beta-h57-597>

anti-CD8a (1:500, 53-6.7, APC-Cy7, ThermoFisher, Waltham, MA) <https://www.thermofisher.com/antibody/product/CD8a-Antibody-clone-53-6-7-Monoclonal/17-0081-82>

streptavidin antibody (1:1000; 405237, SAV Alexa 647, Biolegend, San Diego, CA), <https://www.biolegend.com/en-us/products/alex-fluor-647-streptavidin-9305?GroupID=GROUP23>

Animals and other organisms

Policy information about [studies involving animals](#); [ARRIVE guidelines](#) recommended for reporting animal research

Laboratory animals Male, C57BL6 Mus Musculus, 3-11 weeks age range

Wild animals No wild animals were used

Field-collected samples No field-collected samples were used

Ethics oversight All experiments were performed with the approval of Caltech IACUC.

Note that full information on the approval of the study protocol must also be provided in the manuscript.

Flow Cytometry

Plots

Confirm that:

- The axis labels state the marker and fluorochrome used (e.g. CD4-FITC).
- The axis scales are clearly visible. Include numbers along axes only for bottom left plot of group (a 'group' is an analysis of identical markers).
- All plots are contour plots with outliers or pseudocolor plots.
- A numerical value for number of cells or percentage (with statistics) is provided.

Methodology

Sample preparation

Spleens or brain tissue dissections of the PVT, hypothalamus, cerebellum or cortex were collected. Single cell suspensions were generated by passing the tissue through a 100μm cell strainer (Corning, Corning, NY) with syringe plunger and rinsed with HBSS (Corning, Corning, NY) containing 10% FBS (Gibco, Life Technologies, Thermo Fisher Scientific, Waltham, MA). Red blood cell lysis was performed (Sigma, St. Louis, MO), diluted with HBSS 10% FBS, and tissue suspension was spun at 350xg for 5 minutes at 4°C. For brain regions, papain digestion in 1ml [200U papain, 0.1mg/ml DNase I] was performed for 20 minutes at 37°C, samples were triturated gently through a 1000ul pipette tip, and then passed through a 40μM filter. Samples were then mixed with 5-10 mls of 25% percoll in HBSS and spun at 1000xg for 25 minutes in a swinging rotor. Myelin debris layer was aspirated from the top, cell pellet was washed in HBSS 10% FBS and then resuspended in HBSS buffer containing Fc block (Anti-Mo CD16/CD32, Ebioscience, San Diego, CA; Invitrogen, Carlsbad, CA) for 20 minutes at 4°C. Primary stains and antibodies included: Aqua Dead cell stain (Thermo Fisher Scientific, Waltham, MA), anti-NG2 (1:400; Alexa488; 53-6504-80, Ebioscience, San Diego, CA) and anti-MOG (1:100; biotinylated, BAM2439, Novus Biologicals, Littleton, CO), and were incubated with cells for 30 minutes at 4°C. After washing, secondary streptavidin antibody (SAV Alexa 647, 405237, Biolegend, San Diego, CA), was incubated with cells for 30 minutes at 4C. After washing, cells were fixed with 2% PFA for 20 minutes, washed, and analyzed on a 4 laser (Violet, Blue, Yellow, and Red) CytoFLEX S Flow Cytometer in the Caltech Flow Cytometry Core Facility.

Instrument

CytoFLEX S Flow Cytometer

Software

CytoFLEX S Flow Cytometer and FlowJo was used for the collection and analysis of flow cytometry data

Cell population abundance

Only dead cells, doublets and debris were removed from the gating strategy shown in Figure 3H.

Gating strategy

Gating strategy was determined using unstained and single color stained controls. Cells were gated to avoid debris, along with gating on single cells, Aqua dead cell stain, and NG2-488 and MOG-biotin + SAV-647 positive cell populations.

Tick this box to confirm that a figure exemplifying the gating strategy is provided in the Supplementary Information.

Magnetic resonance imaging

Experimental design

Design type

Intergroup differences of diffusion MRI tract-based measures

Design specifications

Source of data: (ex vivo diffusion MR histology) and analysis: (differences in tract-based diffusion parameters derived from single fiber tractography constrained by a single ROI). Between group effect size calculated for derived diffusion parameters.

Behavioral performance measures

None - all MRI was performed on ex vivo brains

Acquisition

Imaging type(s)

Diffusion Weighted imaging

Field strength

7.0 T

Sequence & imaging parameters

A Bruker standard DWSE (diffusion weighted spin echo) sequence was used to collect images with b value of 4000 s/mm², gradient duration=5.6 ms, gradient separation=12.54 ms, repetition time TR=200 ms, echo time TE=23.34 ms. T1 and T2 weighted images were also collected using standard Bruker sequences (T1_FLASH_3D, T2_TurboRARE). Isotropic image resolution was fixed for all scanning at a field of view (FoV)= 14 mm and a resolution of 175 μ m at each dimension.

Area of acquisition

whole brain

Diffusion MRI

Used

Not used

Parameters All MRI scans were performed using a Bruker Avance Neo 7T/30 scanner and a Bruker gradient and shim unit (B-GA12SHP insert for BGA20) supported by a Bruker PV360 software package. A Bruker quadrature volume coil (B-GA12s HP) and a mouse brain 2x2 receive-only four element array coil were used for 1H RF pulse transmission and signal receiving, respectively, at its operating frequency of 300.33 MHz. b value of 4000 s/mm² (also tested for other lower values), gradient duration=5.6 ms, gradient separation=12.54 ms, repetition time TR=200 ms, echo time TE=23.34 ms, and using 60 gradient different directions.

Preprocessing

Preprocessing software

DSI Studio software package (<http://dsi-studio.labsolver.org/>) for reconstruction and track calculations and statistics

Normalization

All normalization was performed within the DSI Studio software: a Bruker image file is introduced without no image resampling, and a nonlinear registration process is performed from a FIB file that was reconstructed using GQI (generalized q-sampling) with ODFs to allow running atlas-based fiber tracking calculation around a ROI. A T1W image was inserted to use rigid body transformation.

Normalization template

CIVM Template (Duke)

Noise and artifact removal

To our best knowledge, there is no noise and artifact removal step performed in DSI Studio software for animal image data.

Volume censoring

As far as the DSI Studio software handles the reconstruction, there was no dropped case. The calculated fiber tracks, however, were diverse among mouse brains tested. Most of DWI images passed to produce fiber tracks of ROIs we tested. Some DWI images with poor SNR did not produce enough tracks with a threshold used, which was deselected during our t-statics test.

Statistical modeling & inference

Model type and settings

Simple difference of mean FA within each tract

Effect(s) tested

Difference of tract-base mean diffusion metrics due to treatment/modification

Specify type of analysis: Whole brain ROI-based Both

Anatomical location(s) Individual ROI (i.e., PVT) was calculated using the implemented routine under CIVM mouse atlas (Duke radiology, <https://www.civm.duhs.duke.edu/>)

Statistic type for inference
(See [Eklund et al. 2016](#))

No null-hypothesis based inference performed. Effect size of FA differences (Cohen's d) reported.

Correction

None

Models & analysis

n/a	Involved in the study
<input checked="" type="checkbox"/>	Functional and/or effective connectivity
<input checked="" type="checkbox"/>	Graph analysis
<input checked="" type="checkbox"/>	Multivariate modeling or predictive analysis